

Master's Thesis

In situ testing of composite materials using synchrotron X-ray microtomography

Eonyeon Jo

Department of Mechanical Engineering

Graduate School of UNIST

2018

In situ testing of composite materials using synchrotron X-ray microtomography

Eonyeon Jo

Department of Mechanical Engineering

Graduate School of UNIST

In situ testing of composite materials using synchrotron X-ray microtomography

A thesis/dissertation
submitted to the Graduate School of UNIST
in partial fulfillment of the
requirements for the degree of
Master of Science

Eonyeon Jo

12. 07. 2017

Approved by



Advisor

Wooseok Ji

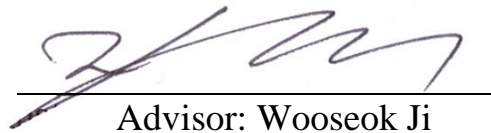
In situ testing of composite materials using synchrotron X-ray microtomography

Eonyeon Jo

This certifies that the thesis/dissertation of Eonyeon Jo is approved.

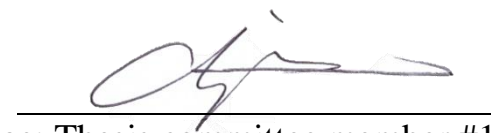
12. 07. 2017

Signature



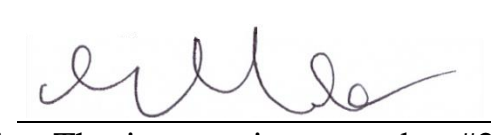
Advisor: Wooseok Ji

Signature



Han-Gi Chae: Thesis committee member #1

Signature



Jae-Hong Lim: Thesis committee member #2

ABSTRACT

Composite materials receive increasing attentions from various industrial sectors including aerospace, automotive and marine industries owing to the specific weight advantages. However, due to their unique heterogeneity, the composite materials suffer from various failure modes at multiple length scales. At the micro level, matrix microcracking, fiber/matrix debonding, and fiber breakage are typically observed. These micro-failure modes may occur at a very low stress, and as load increases they grow into a larger scale mode of failure such as transverse matrix cracks at the meso-length scale and delamination at the macro-length scale. In order to have a better understanding of how a composite structure fails, it is essential to closely examine the growth and interaction of the various failure modes at the micro-length scale first.

This thesis presents *in situ* tests on composite materials using synchrotron X-ray microtomography that can reveal subsurface material behavior in real time. Since the micro-failure modes are initiated and growing inside of the composites, conventional *ex situ* and non-destructive testing protocols are insufficient to obtain detailed information about the initiation of various failure modes and their interactive mechanisms as they grow. In this thesis work, two unique experimental configurations have been developed to observe subsurface failure behavior of a uni-directional continuous fiber reinforced composite with epoxy as a matrix material and a ceramic matrix composite (CMC).

Using the uni-directional continuous fiber reinforced epoxy composite material, two types of laminated composite panels were fabricated and tested. $[+45_2/-45_2]_S$ specimens were utilized to monitor the initiation and evolution of matrix microcracks, which is the main cause of stiffness degradation in laminated composite structures. $[90_2/0_2]_S$ specimens with a single-edge notch were tested to study interactive mechanisms between various failure modes. A special tensile loading stage was developed to apply tensile loading to the specimens, while X-ray scanning was being processed. X-ray microtomography have facilitated the visualization of the complex failure progression occurring inside the specimens as well as the quantification of the subsurface fracture behavior.

It is well known that CMC materials have a unique microstructure consisting of ceramic matrix, ceramic fibers and coating layers surrounding each fiber. Thermomechanical

behavior of the complex microstructure was investigated at an elevated temperature. Another tensile loading stage installed with a heating chamber was designed and fabricated to apply thermomechanical loading to the CMC specimens. The heating chamber used four halogen lamps to heat up the specimen up to 1200 degrees Celsius. The internal responses of the CMC specimens at various loading and temperature conditions were recorded using the X-ray tomography. The maximum loading and temperature simultaneously applied to the specimen were 0.9 kN and 1190 degrees Celsius, respectively.

TABLE OF CONTENTS

Chapter	Page
ABSTRACT	v
TABLE OF CONTENTS	vii
LIST OF TABLES	ix
LIST OF FIGURES	x
CHAPTER 1: Introduction	1
1.1. Introduction.....	1
1.2. Organization of the thesis	4
CHAPTER 2: In situ tests on FRP	5
2.1. Introduction.....	5
2.2. Design and fabrication of an in situ device.....	6
2.2.1. Overview of the in situ mechanical loading device.....	6
2.2.2. Mechanical loading system with a stepper motor	8
2.2.3. Load measuring system with a load cell.....	9
2.2.4. Performance test of the loading device using finite element analysis	11
2.3. Test specimens for in situ experiments.....	13
2.4. In situ mechanical testing with X-ray tomography.....	15
2.4.1. Comparison of X-ray sources	15
2.4.2. In situ experiments using laboratory X-ray source.....	17
2.4.3. In situ experiments using a synchrotron light source	21
CHAPTER 3: In situ thermomechanical tests on CMCs	28
3.1. Introduction.....	28
3.2. Design and fabrication of a high temperature in situ device	29
3.2.1. Overview of the thermal/mechanical loading device	29
3.2.2. Mechanical loading system	31
3.2.3. Thermal loading system.....	32
3.2.4. Specimen grip system.....	36

3.3. CMC specimens	37
3.3.1. Examination of the specimen	37
3.3.2. Specimen fabrication for in situ tests	38
3.4. Thermal/mechanical tests with X-ray synchrotron	39
3.4.1. In situ thermal loading test	39
3.4.2. In situ thermomechanical loading test	42
CHAPTER 4: Conclusion	46
4.1. Conclusion	46
4.2. Novelty and contribution	46
4.3. Future works	47
REFERENCES	48
ACKNOWLEDGEMENTS	53

LIST OF TABLES

Table	Page
Table 2-1: Mechanical Properties of laminated composite.....	13

LIST OF FIGURES

Figure	Page
Figure 1-1: (a) Fiber-reinforced polymer matrix composite (b) Composite structure composed of multiple layers with different fiber orientations [1]	1
Figure 1-2: Damage progression across multiple length scales.....	2
Figure 2-1: Synchrotron rotation stage [14].....	6
Figure 2-2: Designed and fabricated in situ mechanical loading frame	7
Figure 2-3: The mechanical load control system with a stepper motor and a motion controller.....	9
Figure 2-4: DAQ protocol with a load cell using a custom-built LabView code	10
Figure 2-5: (a) Finite element model of the in situ loading frame (b) Loading condition for FEA	12
Figure 2-6: FEA results for the loading device.....	12
Figure 2-7: Specimen dimensions for (a) [90 ₂ /0 ₂]s and (b) [+45 ₂ /−45 ₂]s (unit: mm).....	14
Figure 2-8: Microscopic observation of the notch surface	15
Figure 2-9: (a) Xradia 520 Versa (b) Pohang Accelerator Laboratory (PAL).....	16
Figure 2-10: X-ray source geometry (a) Cone beam (b) Parallel beam [19]	17
Figure 2-11: In situ mechanical loading system in laboratory-scale X-ray source.....	18
Figure 2-12: (a) Double edge notched specimen geometry (unit: mm) (b) In situ loading steps for [+45 ₂ /−45 ₂]s specimen.....	18
Figure 2-13: Internal crack distribution of the [+45 ₂ /−45 ₂]s specimen when the applied stress is (a) at 30% of σ_{UTS} (b) at 90% of σ_{UTS}	19
Figure 2-14: Single edge notched specimen geometry (unit: mm) (b) In situ loading step for [90 ₂ /0 ₂]s specimen	20
Figure 2-15: Multiple failure modes in [90 ₂ /0 ₂]s specimen with 3D tomography (a) Transverse matrix cracks (b) and (c) Delamination at the interface of 0°/90° plies.....	20
Figure 2-16: (a) Precision rotational/translational stages for the alignment of the specimen to the X-ray beam (b) Schematic illustration of the synchrotron X-ray beam system	22
Figure 2-17: Stress-strain response of [90 ₂ /0 ₂]s specimen with a single edge notch. Points 1 to 9 indicate the load when the X-ray images were taken.	22

Figure 2-18: Example of 2D tomography slice images obtained from the in situ tensile test on [90 ₂ /0 ₂]s specimen with a single edge notch. Multiple failure modes were detected..	23
Figure 2-19: 3D volume image of the unloaded specimen near the notch tip	24
Figure 2-20: 3D volume image of the specimen with various failure modes at different loading steps.....	25
Figure 2-21: 3D volume images with the cracks viewed in the xz-plane.....	26
Figure 2-22: (a) Denotation of each crack (b) Growth of the densities of different transverse matrix cracks (c) Density changes for delamination and splitting failure	27
Figure 3-1: In situ thermomechanical loading frame installed in PAL	30
Figure 3-2: Schematic of the operation principle of the specimen loading system	31
Figure 3-3: Transmission rate as a function of X-ray energy for various path length through an aluminum window [33]	32
Figure 3-4: Components of the heating chamber.....	33
Figure 3-5: Focal heat zone at the center of heat chamber with four lamps	33
Figure 3-6: Temperature measurement in the heat zone (a) Ceramic beaded B type thermocouple (b) Peak temperatures with a variance of input powers	34
Figure 3-7: Pyrometer set up for measuring the temperature of a specimen	35
Figure 3-8: Temperaure easured by pyrometer as a function of power supplied to heating lamps	36
Figure 3-9: Temperature continuity test result over a 2h period	36
Figure 3-10: Specimen holding system with Invar 36	37
Figure 3-11 (a) C/C-SiC: C/C segments (darks), SiC (grey) and silicon (white) [39] (b) SEM result of the present CMC specicmen.....	38
Figure 3-12: Microstrucure of a CMC specimen (a) three-dimensional (b) viewed in the xy plane.....	38
Figure 3-13: Specimen fabrication with a low-speed diamond saw	39
Figure 3-14: Specimen installation for in situ thermal loading test.....	40
Figure 3-15: 2D slice images and 3D CT results from in situ thermal tests	41
Figure 3-16: (a) Fishnet-shape matrix (b) Debris found in the specimen (c) Debris in 3D space.....	42
Figure 3-17: Specimen loading for in situ thermal/mechanical loading test	43

Figure 3-18 Measured compressive load during X-ray scanning (a) 200N (b) 910N	43
Figure 3-19: Fully 3D tomography results of in situ thermal/mechanical loading test	44
Figure 3-20: 2D slice images result of the in situ thermal/mechanical tests (a) specimen movement (b) selected characteristic images	45

CHAPTER 1: Introduction

1.1. Introduction

The overall objective of the thesis is to develop a novel testing and visualization technique to characterize complex and interacting failure modes observed in a composite material under thermal/mechanical loading. A composite material is composed of more than two materials to achieve desired properties that cannot be obtained from a monolithic material. As shown in Figure 1-1(a), a lamina consisting of a polymer matrix reinforced with unidirectionally continuous glass or carbon fibers is typically used to construct a laminated composite structure as shown in Figure 1-1(b). Such composite structures are increasingly used in commercial and military aerospace applications owing to their specific weight advantages.

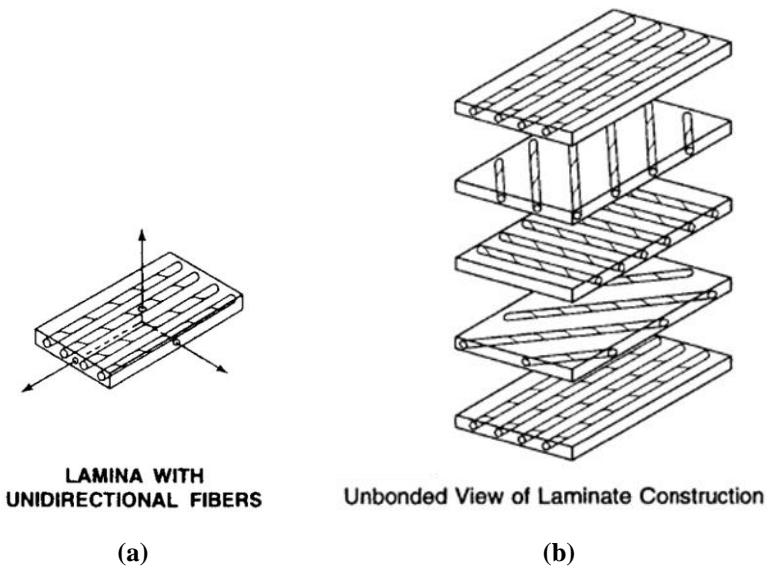


Figure 1-1: (a) Fiber-reinforced polymer matrix composite (b) Composite structure composed of multiple layers with different fiber orientations [1]

However, the unique microstructure of the composite may induce micro damage and failure at the fiber length scale mainly because of the significant stiffness mismatch between the reinforcement and matrix. Homogenized manifestations of the micro-scale deficiencies can be coupled to the higher length scales that may lead to catastrophic failure of an entire structural system. Figure 1-2 schematically illustrates the failure progression

typically observed in the composite material from the microscale to the macroscale. Figure 1-2 shows a laminated composite structure composed of two layers with different fiber orientations. A 90-degree layer is placed on a 0-degree layer. Fibers are colored in gray while matrix is displayed in white. As shown in Figure 1-2 (a), the microcracks is prone to occur initially in the matrix phase since the matrix material is typically weaker than the fiber constituent. As the structure is more loaded, the matrix microcracks grow into the transverse cracks as shown in Figure 1-2 (b). The transverse cracks can cause the interfacial failure, which is typically called delamination. As can be seen in Figure 1-2, the micro damage can cause other failure modes at the higher length scale and thus detailed physics of damage progression and failure mechanisms at the micro-length scale in the composite material should be carefully characterized

Although many researches have been performed to characterize damage and failure at the micro-length scale, they rely on hypothetical theories based on the observation of failure patterns from tested specimens. Detailed processes that lead to the final failure pattern are extremely difficult to obtain without a special testing instrument equipped with a microscopic device. Digital image correlation (DIC) technique is now widely used to investigate the progressive damage and failure response of composite materials, but the information obtained from DIC is also limited to surfaces where speckle patterns are applied.

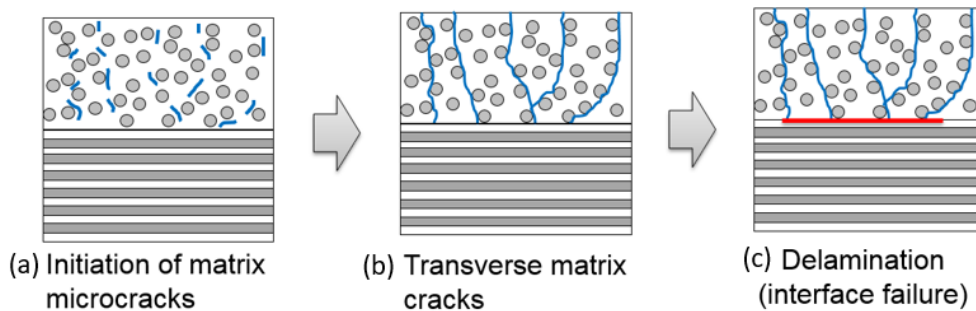


Figure 1-2: Damage progression across multiple length scales

With the increasing interest in microscale experiments and the development of computational tomography resources, 3D X-ray micro-computed tomography (μ CT) has been utilized recently to visualize microstructural behavior in composite materials. X-ray tomography has evolved into a powerful imaging tool in the fields of physical and

biological sciences from its ability to image structure in three dimensions with high spatial resolution at macroscopic to submicroscopic scales [2-3]. Buffiere et. al. compared advantage and limitations of laboratory-scale and synchrotron X-ray sources for *in situ* thermal/mechanical testing [4]. Team of Spearing performed tensile test on [90/0]s laminates using a synchrotron X-ray source and revealed the progression of different failure modes and their interactions [5-7]. Garcea et. al. further developed the work by Moffat et. al. by applying fatigue loading on the specimens with the same configuration [8]. Hufenbach et. al. built a laboratory-scale X-ray tomography system and carried out tensile and compression tests on woven composite [9]. Bale et. al. observed failure events in ceramic matrix composites under combined mechanical and elevated temperature loading using a synchrotron X-ray [10]. Sket et. al. utilized $\pm 45^\circ$ carbon fiber reinforced laminates to investigate damage progression in matrix [11]. All the test results successfully visualized micro features as thermal/mechanical loading is applied, but the quantification of specific damage and failure modes are not linked with either applied loading data. None of the aforementioned tests did not utilize the 3D tomography results to investigate the interaction and effect of various failure on the subsurface of composite materials.

In this thesis, an experimental technique has been developed that is capable of characterizing and quantifying the progression of damage and failure inside composite materials at micro-scale in a fully three-dimensional (3D) setting. *In situ* testing of composite materials using synchrotron X-ray μ CT have been conducted for the visualization of damage progression and interactions of various failure modes. Small-scale *in situ* mechanical loading devices have been designed and fabricated for the experimentation. Two types of loading devices operating at a room temperature and an elevated temperature have been built to observe subsurface failure behavior of two different composite materials; a uni-directional continuous fiber reinforced composite with epoxy as a matrix material tested at a room temperature and a ceramic matrix composite (CMC) at a high temperature. Both of the devices are specifically designed to be mounted on the synchrotron stage of the beamline 6C in Pohang Accelerator Laboratory (PAL). The beamline 6C is equipped with various X-ray detectors with the field of view (FOV) of 7 cm \times 7cm, 6 cm \times 4 cm and less than 7 mm \times 5 mm. The pixel size corresponding to each

FOV size are 48, 32 and 1-5 microns, respectively [12]. According to specimen types and experimental circumstances, an appropriate setting has been selected to obtain desired information.

1.2. Organization of the thesis

This thesis consists of two main parts based on the types of composite materials. Chapter 2 is concerned with the fiber-reinforced polymer (FRP) composites and Chapter 3 deals with the CMC material. Chapter 2 begins with the development of the *in situ* mechanical loading device and unique features of the equipment are presented. FRP specimens with various stacking sequences are tested to observe various subsurface failure modes. In this chapter, especially, both laboratory-scale and synchrotron X-ray sources have been utilized. Pros and cons of each X-ray source are briefly discussed. X-ray tomography results show detailed damage progression inside the FRP specimens. Cracks are individually segmented and their length are measured as they grow with an increasing load.

Chapter 3 also begins with describing the development of a loading frame with a heat chamber for testing the CMC at a high temperature. The maximum loading and temperature that can be applied to the specimen are 1 kN and 1200°C, respectively. *In situ* tests are conducted at various loading and temperature conditions in order to have a reference data, X-ray scanning of the specimen is conducted at a room temperature first. Next, the CMC specimen are scanned at 900°C and 1190°C without any mechanical loading. Thermomechanical *in situ* test is conducted at a constant temperature of 1190°C, with a variant of mechanical loading. Final conclusion and a summary of findings are presented in Chapter 4 along with suggestions for future works.

CHAPTER 2: *In situ* tests on FRP

2.1. Introduction

This chapter describes experimental tasks performed to characterize the unidirectional continuous fiber reinforced composite, using X-ray tomography. Three major tasks were carried out and they are:

- Design and fabrication of an *in situ* device
- Mechanical testing on the unidirectional continuous fiber reinforced composite
- *In situ* mechanical testing with X-ray tomography

In situ mechanical tests on a unidirectional fiber-reinforced polymers (FRP) has been performed. Matrix damage progression in FRP has been investigated with a double-edge notched specimen in $[+45_2/-45_2]_S$ laminates. Single-edge notched specimen with the layup sequence of $[90_2/0_2]_S$ was utilized to observe the interactive subsurface damage and progression under tensile loading. Special loading frame was designed and fabricated for the *in situ* test at a synchrotron facility. Three-dimensional tomography images show multiple failure modes occurring sequentially as the applied load increases. In this chapter, the interactive failure mechanism under the surface of the composite materials has been revealed.

In this chapter, both laboratory-scale and synchrotron X-ray sources have been utilized to assess damage progression and identification of initiation and interaction of various failure modes. Laboratory-scale X-ray microscope, ZEISS Xradia Versa, is utilized for the *in situ* test with $[+45_2/-45_2]_S$ specimen. The equipment is available in Korea Institute of Science and Technology (KIST), which is a nation-operated research organization. Versa is capable of mounting a bigger specimen in the scanning bed than other similar μ CT devices with a voxel size ranging from 0.1 to 100 microns [13]. Also, the synchrotron X-ray microscope available in Pohang Accelerator Laboratory (PAL) have been utilized. *In situ* mechanical test with $[90_2/0_2]_S$ specimen have been performed at the beam line 6C on PAL where the designed loading frame can be set up.

2.2. Design and fabrication of an *in situ* device

2.2.1. Overview of the *in situ* mechanical loading device

A special load frame for performing *in situ* mechanical tests in an X-ray synchrotron beamline was designed and fabricated. The loading device was designed such that it can be mounted on a high precision rotation stage (EN-409, XHUBER Inc. [14]) that is installed in the X-ray tomography beamline (Beamline 6C) at PAL (see Figure 2-1). In order to precisely control an elaborate movement of the rotation stage, the weight of loading device did not exceed 20 kg, which is required by the specification of the stage. In addition, the height of the loading device was determined by accounting for the focal position of the X-ray beam when the device was placed on the optical table in the Beamline 6C. As a result, a small-scale loading frame was designed and fabricated as shown in Figure 2-2. The axisymmetric shape of the device was preferred for the reduction of moment of inertia when the stage is rotating to take X-ray images.

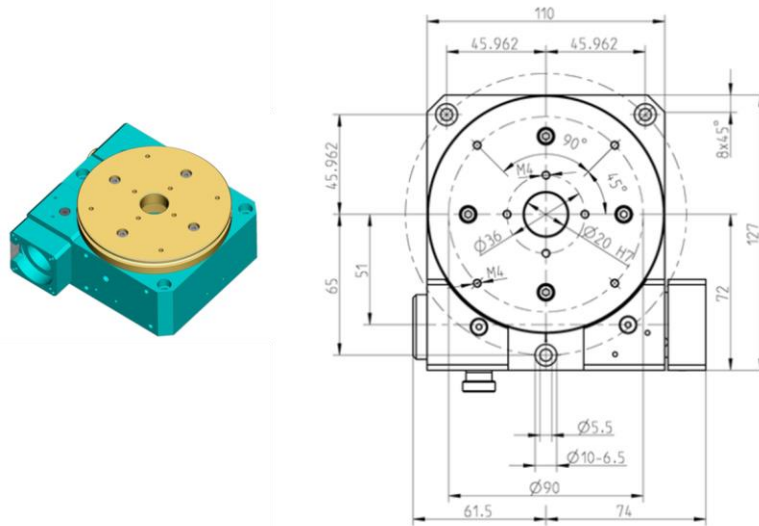


Figure 2-1: Synchrotron rotation stage [14]

Data obtained from *in situ* experiments for a composite material with X-ray tomography are basically three-dimensional images that reveal subsurface behavior of the material under a certain loading condition. When X-ray beams penetrate through a specimen, the intensities of the beams are altered because of different attenuation rates of fibers and a matrix. These changes are collected and recorded using a detector and used

later to reconstruct 3D images of the subsurface structure of the composites material. Therefore, it is crucial to clear the pathways of X-ray beams. The loading frame, however, had a tube surrounding the specimen as shown in Figure 2-2. The tube was an unavoidable feature for the loading frame because it connected upper and lower parts and protected the beamline from any debris that may fall off during a test. It is important to note that a polymethyl methacrylate (PMMA) material was used which is transparent and has a low density. PMMA is known as no effect on the changes in the intensity of X-ray beams.

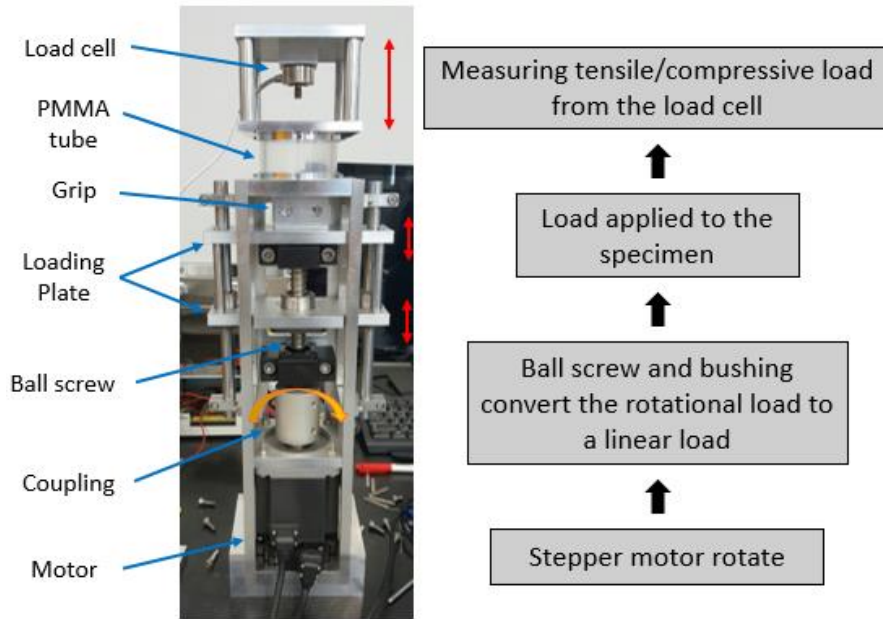


Figure 2-2: Designed and fabricated *in situ* mechanical loading frame

According to the principle of X-ray tomography, distance between a sample and a detector greatly affects the final quality of images. It is typically recommended that the distance be as short as possible for reducing loss in image quality. For this reason, the diameter and the thickness of the PMMA tube were carefully selected so that it would have not been an obstructive factor in obtaining X-ray images. On the other hand, it was desirable to have as thick PMMA tube as since the tube was also a support structure while loading was applied to the specimen. We found the optimal thickness for the tube that could endure the highest induced-loading without sacrificing image quality too much. The relationship between a transparent rate and a thickness of PMMA was identified based on the reference transparent rate data of the X-ray instrument at PAL, using a demo program.

Lastly, we polished the surface of the PMMA tube with a very fine grit to improve the poor surface condition after the tube was machined from a lathe.

3D tomography images of carbon-reinforced polymer undergoing mechanical loading were obtained from sets of X-ray projection images (radiographs) recorded as the test instrument is rotated stepwise through an angular range of 180°. Specimens were held between grips connected to a motorized loading fixture that loads the samples in tension or compression. Axial deformation of the specimen was measured from encoder imbedded in the stepper motor. A ball screw and busing parts convert rotational energy from stepper motor to linear loading force on specimen. Applied load to the specimen was measured through a piezo-electric type load cell (Model-31-mid, tension/compression up to 1000 lbf, manufactured by Honeywell [15]) that was installed in the top part of the devise as shown in Figure 2-2.

2.2.2. Mechanical loading system with a stepper motor

The mechanical loading system of the *in situ* loading device consisted of a stepper motor and a linear actuator system including a ball screw to apply. Considering typical material properties of composites materials, the loading system was designed to deliver an axial load of up to 5 kN on the specimen. The required torque of a stepper motor to achieve the desired load capacity can be calculated from

$$T = \frac{\mu N P_B}{2\pi R\eta} \quad (2-1)$$

where T is the torque from a motor, μ is the frictional coefficient of a sliding surface, N is the force in a moving direction, P_B is the ball screw lead, R is the gear ratio and η is the efficiency of a stepper motor. When $N= 5$ kN, the preferred motor capacity was found to be 0.314 N · m. The stepper motor (MR-J4-KR-73, Mitsubishi Corp. [16]) chosen for the loading device based on the calculation has a rated torque of 2.4 N · m, which is a sufficient loading capacity to perform mechanical testing on composite materials. The stepper motor was directly connected to a ball screw through a coupling as shown in Figure 2-2. The motor drove the precision ball-screw that converted a rotational kinetic energy from a motor to a linear motion.

The motor control system was also constructed to apply a specific loading rate to a specimen. Figure 2-3 schematically shows the control system. The loading control system consisted of a PCI-type motion controller (NI-PCI-7332, National Instruments Corp. [17]), an input signal generator and a motor driver to precisely control a desired loading rate. When a specific loading rate was determined by a user, pulse signal was generated from the generator for an input command to the motor. Then the motor driver as shown in Figure 2-3 received the input signal and operated the motor. Axial displacement due to the rotation of the motor shaft was measured by a high-resolution encoder (4M pulses/rev). By multiplying the number of rotations and pitch of the ball screw, the axial displacement was obtained. The motion controller based on the PID controller carried out a feedback control on the motor to achieve the specific loading rate given in axial displacement per minute.

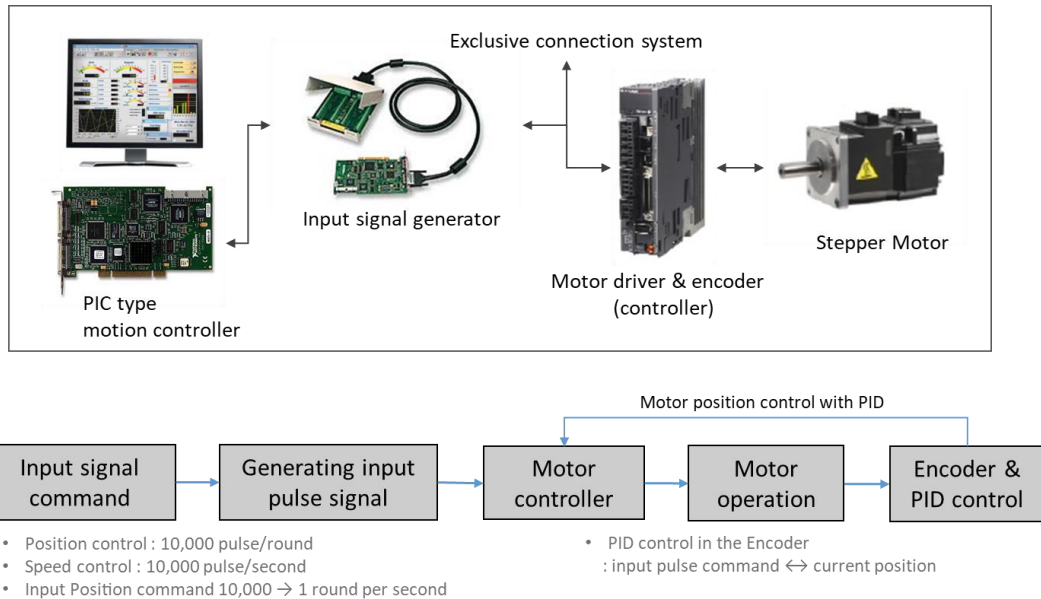


Figure 2-3: The mechanical load control system with a stepper motor and a motion controller

2.2.3. Load measuring system with a load cell

A data acquisition (DAQ) system was developed on the National Instruments LabView platform [18] as shown in Figure 2-4. The DAQ system collected load and displacement data during *in situ* tests and the load-displacement curve was used to closely investigate progressive failure behavior of the composite material in conjunction with X-ray tomographic images. Detailed discussion about the progressive failure mechanism will be

explained in the later section. Axial displacement data were obtained from the encoder as described in the prior section and the load data was obtained from a load cell installed in the loading device as shown in Figure 2-2.

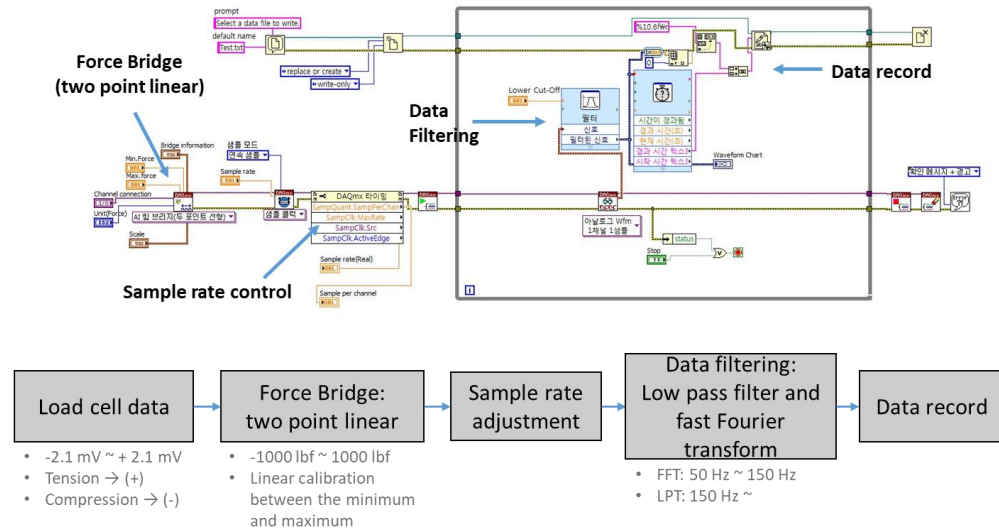


Figure 2-4: DAQ protocol with a load cell using a custom-built LabView code

The load cell was selected accordingly based on the maximum load capacity from the stepper motor that was computed as described in the prior section. The measurement range was the first criterion in selecting the load cell. In addition to the measurement capacity, the mass and size of the load cell were accounted for because of the limitation on the overall size and weight of the *in situ* loading device. A piezo-electric type load cell (Model-31-mid, up to ± 1000 lbf, Honeywell [15]) was chosen and installed in the top part of the loading frame to measure forces applied on the specimen.

The DAQ board (cDAQ-9174 and NI9237, compact 24bit bridge analog input module, NI [17]) was implemented to collect milli-volt output signals coming out from the load cell. The raw signals were mixed with inevitable noise since the voltage lever was too low. Thus, in order to suppress the noise, we used two filters; the low path filter and the fast Fourier transform (FFT) filter. Through the low path filter, the array of signals below 150 Hz was removed. In addition, the noise in the range of 50 to 150 Hz was handled with the FFT filter. After the clean signals were collected, the custom-built LabView program [18] as shown in Figure 2-4 converted the signals into load data and they were visualized. The load data was calibrated from the electric signals based on the two-point bridge method. The

minimum electrical signal of the load cell (-2.1 mV) was corresponding to the minimum load of -1000 lbf and the maximum signal correlated with the maximum load value of 1000 lbf. The LabView program [18] also averaged the load data in every one second interval to eliminate the effect of highly fluctuating signals at a very low level and obtain a reasonable size of data for static test.

2.2.4. Performance test of the loading device using finite element analysis

Finite element analysis (FEA) was carried out to figure out whether the *in situ* loading device performed as expected since experiments at the synchrotron facility had to be done in a limited time. FEA results were also instrumental to improve the design of the loading device. The major design criteria of the loading device were determined because the device had to be successfully implemented into the synchrotron beamline. The precision rotation stage restrained the weight of the loading device. Thus, the overall structure of the loading device was made of light materials and cut off as many non-functional areas as possible. However, thin structures were likely to deform when loading was applied. In addition, the X-ray beam path put on a limitation on both the device height and the material around the specimen. The penetrable PMMA tube was ideal for an X-ray transmission window but the material was not strong enough to be used as a supporting structure. For these reasons, the loading device possessed several potential compliance factors. FEA was conducted to exactly identify the sources of the compliance factors and optimize the device design.

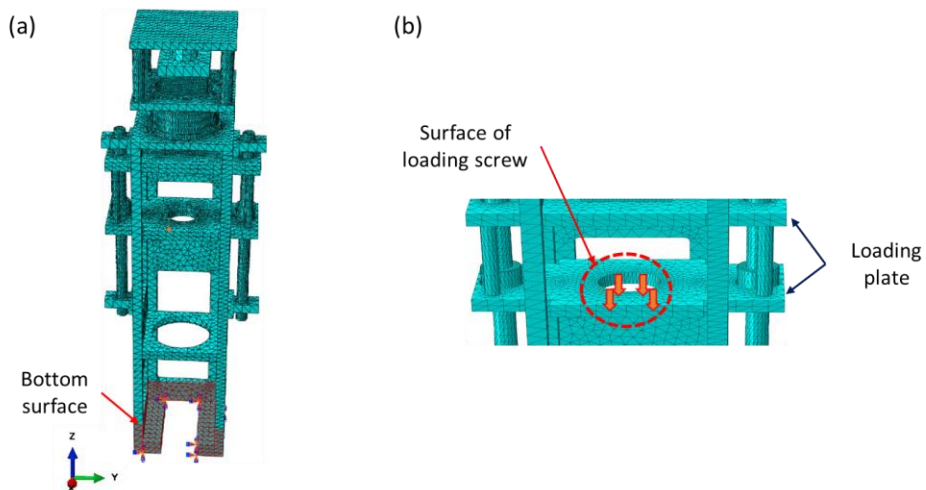


Figure 2-5: (a) Finite element model of the *in situ* loading frame (b) Loading condition for FEA

Figure 2-5 shows the finite element (FE) model of the *in situ* loading frame. For simplification, fastening holes with fasteners were not accounted for in the FE model. The stepper motor and a loading screw were also not considered in the model as shown in Figure 2-5. The FE model was meshed using C3D4 elements. Figure 2-5 (b) shows the loading condition of the model that represents the force applied by the ball screw as the motor operates. In the FE model, the load was applied by specifying a displacement. Degree of freedom (DoF) of the bottom plate were fixed as shown in Figure 2-5 (a) since the plate was fastened onto the rotation stage. Static analysis was conducted using ABAQUS 6.14.

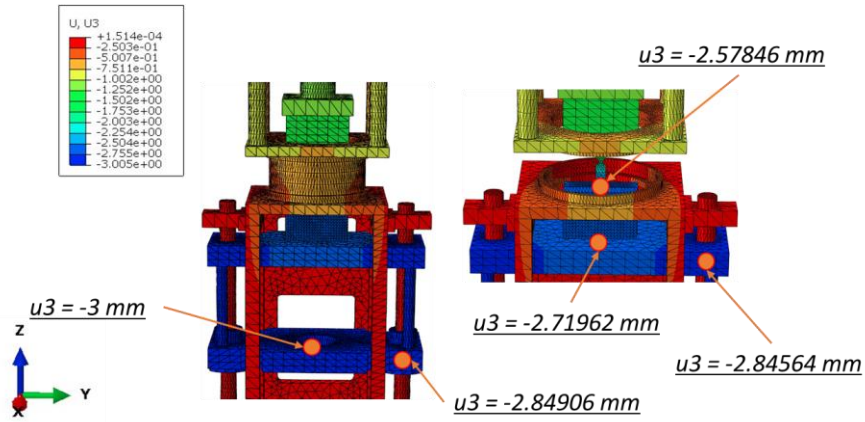


Figure 2-6: FEA results for the loading device

Figure 2-6 shows the FEA result with the axial deformation in the loading direction in the regions of interest. Loading directional (z -directional) displacement is denoted as U_3 and a millimeter scale is used to express the displacement in the results of FEA. As the specified displacement of 3 mm was applied to the loading plate, the specimen was stretched by 2.58 mm. This is mainly because the bending deformation of the loading plate and the deformation of the PMMA tube. For the information, the loading plate was made of SUS304, of which the modulus is 193 GPa. The thickness of the lading plate was 15 mm. From the finite element analysis, it was found that the specimen was not stretched as expected, but the discrepancy was acceptable to obtain 3D tomographic images revealing subsurface failure behavior of composite materials.

2.3. Test specimens for *in situ* experiments

Prepreg with a material system of UIN150/H15 was utilized to manufacture specimens for *in situ* experiments. The prepreg was provided from a domestic company, SK chemical group. Laminated composite panels of $[0_8]_T$, $[90_2/0_2]_S$, $[+45_2/-45_2]_S$ and $[0_32]_T$ configurations were first manufactured by laying up prepgs to measure basic material properties of the composite based on ASTM standards. Table 2-1 shows test results with layups and standard types used to obtained specific material properties. These macroscopic properties were used as a reference dataset for the microscropic characterization of composite materials.

	Properties	Values	Layup	ASTM Standard
Stiffness [GPa]	Fiber direction (E_1)	146.45 ± 2.25	$[0_8]_T$	D3039
	Transverse direction (E_2)	7.439 ± 0.047	$[90_8]_T$	D3039
	Poisson's ratio (ν_{12})	0.338 ± 0.050	$[0_8]_T$	D3039
	Shear (G_{12})	4.15 ± 0.40	$[+45_2/-45_2]_S$	D3518
Strength [MPa]	Fiber direction (X)	2672.24 ± 83.61	$[90_2/0_2]_S$	D3039
	Transverse direction (Y)	26.26 ± 2.24	$[90_8]_T$	D3039
	Shear (S)	43.811 ± 1.151	$[+45_2/-45_2]_S$	D3518
Fracture toughness	Mode I (G_{Ic})	0.1696 ± 0.02	$[0_8]_T$	D6671
	Mode II (G_{IIc})	3.269 ± 0.220	$[0_8]_T$	D7905

Table 2-1: Mechanical Properties of laminated composite

After the basic mechanical behavior of the composite were identified as listed in Table 2-1, specimen dimensions for X-ray tomography were determined based on the results. Specimens with a single edge notch were made from the $[90_2/0_2]_S$ panel. Single-edge notched specimens with a stacking sequence of $[90_2/0_2]_S$ were tested to closely investigate the interaction of multiple failure modes near the notch tip. $[+45_2/-45_2]_S$ specimens were utilized to examine the initiation and evolution of matrix microcracks. Double notches were

introduced to intentionally create a region of stress concentration and thus to define a field of view conveniently. The specimen dimensions are shown in Figure 2-7.

Notches were carefully carved to avoid any undesirable initial damage such as delamination and bur that may affect *in situ* test results. Delamination and bur are typically observed when conventional working tools such as drill machine and router are used. In order to minimize initial damage to the specimen yet fabricate a very sharp notch, we utilized micro-resolution waterjet. The nozzle size of the waterjet was 0.35 mm, sufficient to fabricate a sharp notch without causing initial damage to the specimen as shown in Figure 2-8. Although a field of view is typically very small and limited for X-ray tomography, the specimens in Figure 2-7 were very long. Specimen lengths were determined to provide enough gripping area without causing slipping during tension tests.

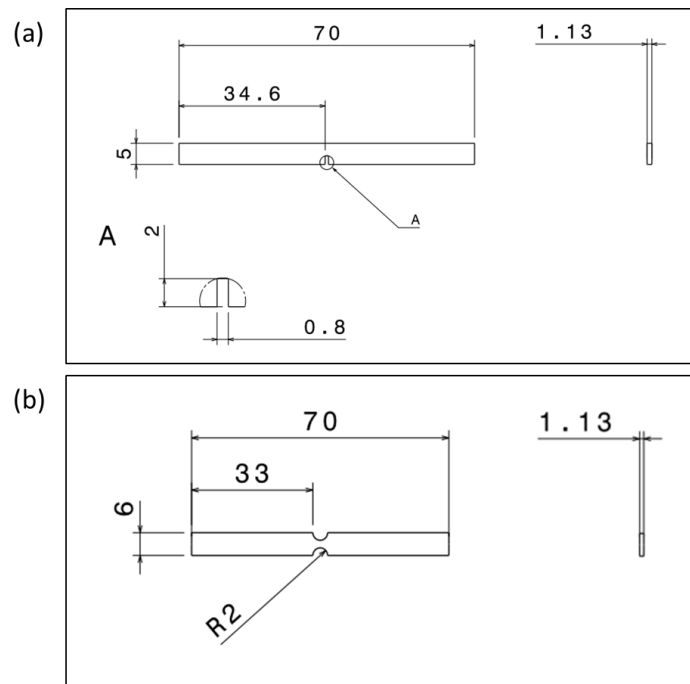


Figure 2-7: Specimen dimensions for (a) [90₂/0₂]s and (b) [+45₂/−45₂]s (unit: mm)

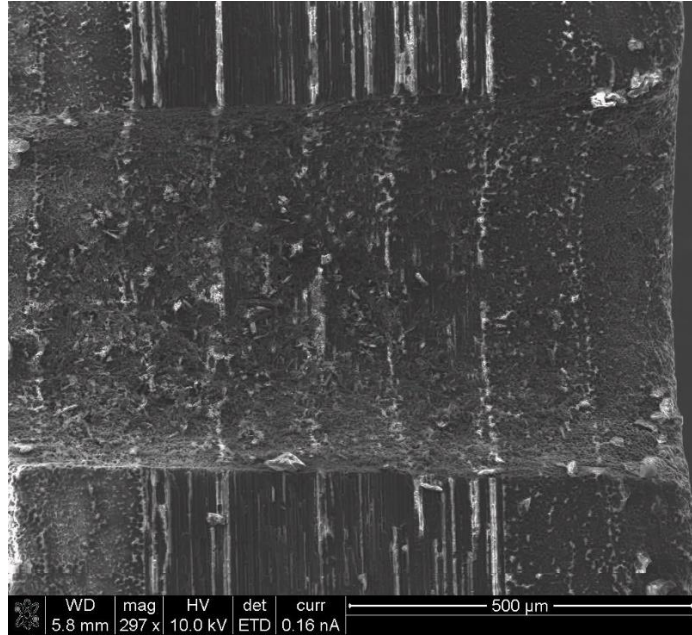


Figure 2-8: Microscopic observation of the notch surface

2.4. In situ mechanical testing with X-ray tomography

2.4.1. Comparison of X-ray sources

Micro-scale damage and failure occurring under the surface of composite materials can be revealed using 3D X-ray microscopic computed tomography (μ CT). *In situ* mechanical testing to examine real-time internal structural response of a material has been typically performed at synchrotron facilities since their test sections are adequate to setup a custom-made loading frame. Pohang Accelerator Laboratory (PAL) (see Figure 2-9(b)) in Korea has the beamline for X-ray μ CT experiments. The detector installed in the PAL beamline has the FOV as large as $1.8 \text{ mm} \times 1.2 \text{ mm}$ and its minimum pixel size is as small as $0.45 \mu\text{m}$.

Current state-of-the-art technology has developed a laboratory-scale X-ray μ CT device. ZEISS Xradia 520 Versa (see Figure 2-9(a)) is the most advanced X-ray μ CT device for *in situ* mechanical testing. Its minimum pixel size is $4.2 \mu\text{m}$ and the field of view (FOV) can be as large as $4.2 \text{ mm} \times 4.2 \text{ mm}$. The device is available in Korea Institute of Science and Technology (KIST) for public use. According to the specification, the synchrotron X-ray beam produce tomographic images with higher resolution than the laboratory-scale X-ray

source. However, the minimum resolution of the laboratory-scale X-ray device is still sufficient to observe micro-scale damage initiation and propagation with much larger FOV. Thus, we have utilized both X-ray types depending on failure modes and desired image resolutions.

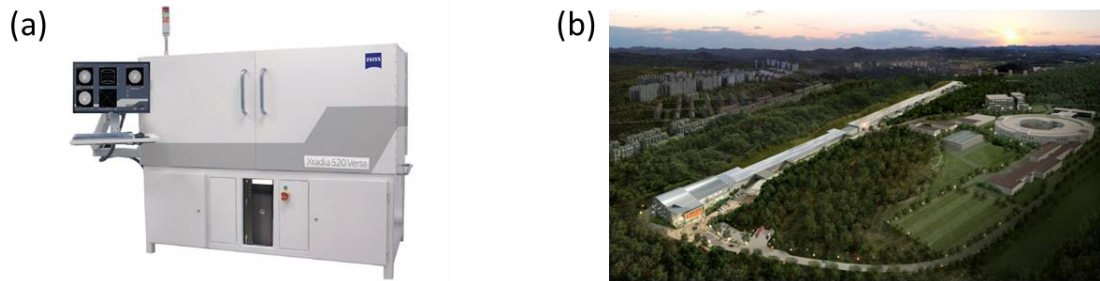


Figure 2-9: (a) Xradia 520 Versa (b) Pohang Accelerator Laboratory (PAL)

The main difference between the laboratory-scale X-ray source and the synchrotron X-ray source is the configuration of the beam as shown in Figure 2-10. Laboratory-scale X-ray μ CT device such as ZEISS Xradia Versa typically uses the cone-beam geometry (see Figure 2-10(a)). The cone beam configuration is commonly employed in most modern medical devices. However, X-ray tomography images using the cone-beam geometry may be distorted depending on the distance between the source and the specimen and the specimen size. Distorted images can be corrected through post-image correction processes to reconstruct realistic 3D configuration of internal structures of specimens. As a result, the quality of final results is greatly dependent on the image correction algorithm. For the information, Xradia Versa, has implemented its own correction process that is disclosed to public. Synchrotron X-ray source uses the parallel beam configuration as shown in Figure 2-10(b). Since the X-ray beams are parallel, tomography images taken at the detector do not suffer from image distortion. Thus, post-image correction process is not required for reconstructing 3D structures of specimens. Furthermore, since the power of the synchrotron X-ray source is much higher than the laboratory-scale X-ray beam, X-ray raw data images from the synchrotron beam are very clear.

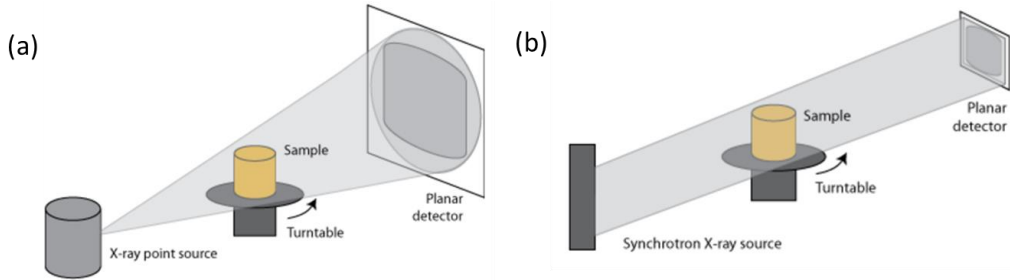


Figure 2-10: X-ray source geometry (a) Cone beam (b) Parallel beam [19]

2.4.2. *In situ* experiments using laboratory X-ray source

A micro-focus X-ray CT system, Xradia 520 Versa, was used to obtain X-ray CT images of internal damage behavior of $[+45_2/-45_2]_S$ and $[90_2/0_2]_S$ composites. $[+45_2/-45_2]_S$ was tested to examine the evolution of matrix microcracks and $[90_2/0_2]_S$ specimens were used to study the interaction of various failure modes. *In situ* mechanical loading experiments were conducted using a commercial loading frame manufactured by DEBEN installed in the testbed of the X-ray device as shown in Figure 2-11. Specimens of both types, $[+45_2/-45_2]_S$ and $[90_2/0_2]_S$, are also shown in Figure 2-11. Aluminum tabs were attached at the both ends of the specimens to firmly fix them in the loading frame. The loading frame with the specimen was mounted on the testbed of the X-ray device and the micro-positioning stage as shown in Figure 2-11 set the desired distance of the specimen with the detector. The distances between the X-ray source, the specimen and the detector are the most important setup parameter because they directly affect the quality of final reconstructed images. As the distance become short, finer resolution can be achieved.

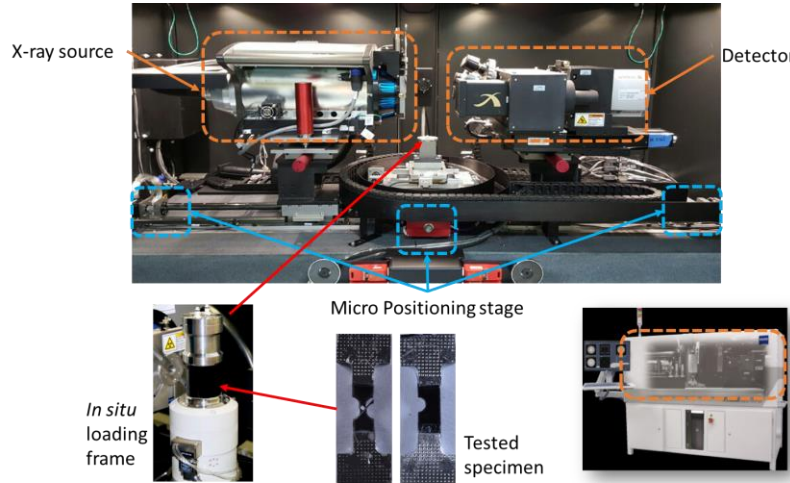


Figure 2-11: *In situ* mechanical loading system in laboratory-scale X-ray source

[+45₂/−45₂]s specimens were manufactured as shown in Figure 2-12(a) to investigate the initiation and propagation of micro damage in the matrix. At the center region of the specimen, round notches were cut to set up a region to observe during the *in situ* experiments. The maximum FOV of the laboratory-scale X-ray device is 4.2 mm × 4.2 mm. the round notches with the radius of 2 mm resulted in the observation region to be 2mm by 2mm, which is smaller than the maximum FOV size. Another important role of the notched at both sides was to raise stresses in the observation region. In this way, internal damage behavior during *in situ* tests occurred first in the observation region.

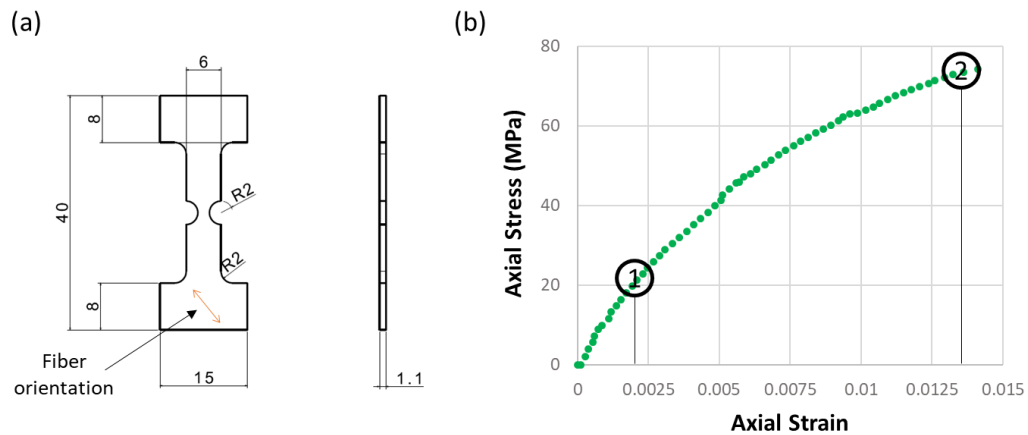


Figure 2-12: (a) Double edge notched specimen geometry (unit: mm) (b) *In situ* loading steps for [+45₂/−45₂]s specimen

As indicated in Figure 2-12(b), X-ray images were taken at two loading cases; 30% and 90% of ultimate tensile stress. When the load reached the desired value, the loading device maintained the load while the micro-positioning stage rotated the specimen to take X-ray radiographs. As a result, total 1600 2D X-ray images were collected per one loading step over the scanning time of around 90 minutes. The collected X-ray scanning images were reconstructed through the Xradia reconstruction program and visualized from the ORS visual software (Object research systems Inc.)

Figure 2-13 shows a rendering of the matrix cracks and their propagation along the fiber direction in the $[+45_2/-45_2]_s$ specimen. Since the fibers are oriented at 45 degrees with respect to the loading direction, the matrix carries almost all the shear loading, leading to the matrix cracks as shown in Figure 2-13. The micro-scale matrix damage was initiated in the notch side (see Figure 2-13(a)). The initiated cracks were then propagated along the fiber direction. As the load reached at 90% of the ultimate tensile stress, both the crack length and density were significantly increased as shown in Figure 2-13(b).

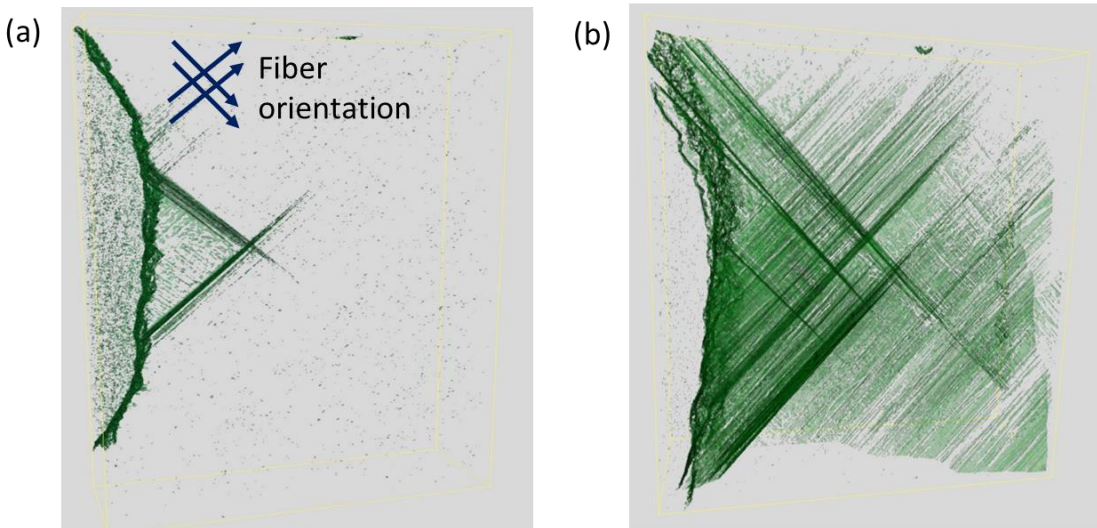


Figure 2-13: Internal crack distribution of the $[+45_2/-45_2]_s$ specimen when the applied stress is (a) at 30% of σ_{UTS} (b) at 90% of σ_{UTS}

Figure 2-14(a) shows the geometry of $[90_2/0_2]_s$ specimens with a single edge notch. The single edge notch was made by a precision water-jet cutting to observe various failure modes. Single edge notch tension (SENT) test was conducted following the similar protocol for the tension tests on $[+45_2/-45_2]_s$ composites. As indicated in Figure 2-14(b),

X-ray radiographs were taken when the load reached at the 70% of the ultimate tensile stress of the [90₂/0₂]s composites measured before the *in situ* experiment was carried out. Figure 2-15 exhibits the 3D tomography of the [90₂/0₂]s specimen loaded at 70% of its strength. Transverse matrix cracks in 90° layers were clearly visualized with the delamination at the interface between 0° and 90° layers. Detailed damage progression for the [90₂/0₂]s specimen with a single edge notch was further studied using the synchrotron X-ray beam

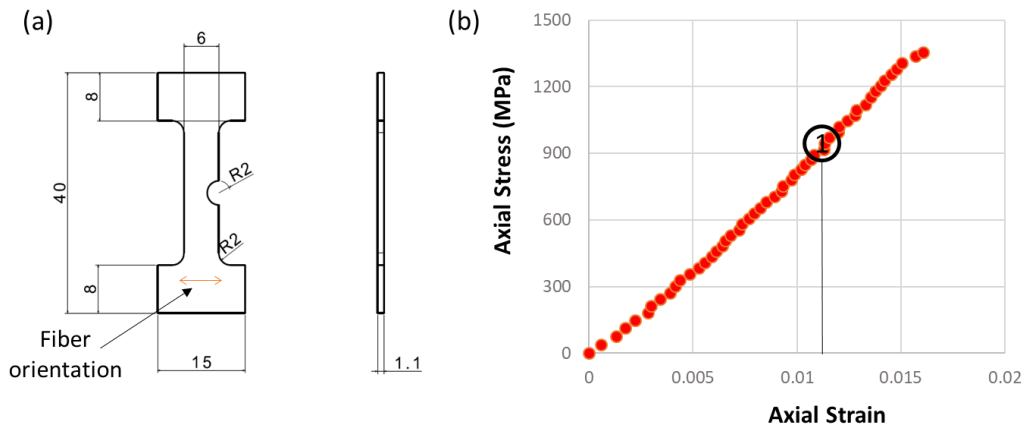


Figure 2-14: Single edge notched specimen geometry (unit: mm) (b) In situ loading step for [90₂/0₂]s specimen

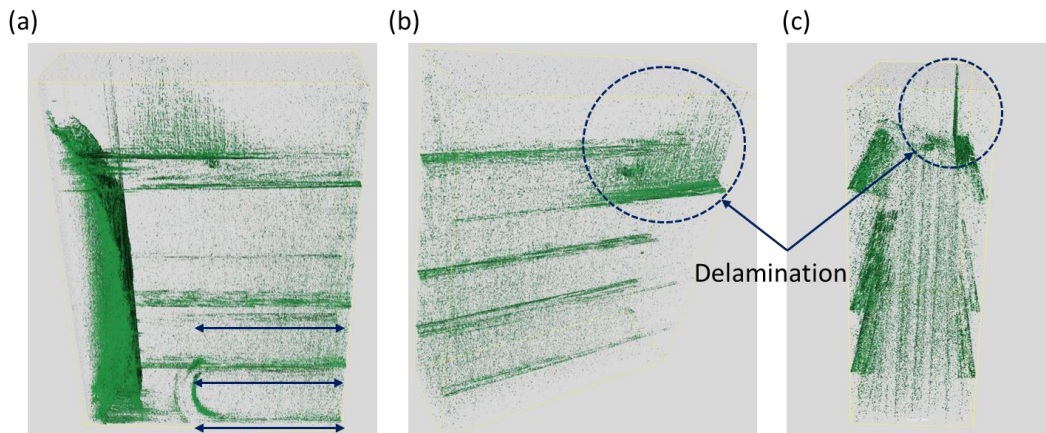


Figure 2-15: Multiple failure modes in [90₂/0₂]s specimen with 3D tomography (a) Transverse matrix cracks (b) and (c) Delamination at the interface of 0°/90° plies

2.4.3. *In situ* experiments using a synchrotron light source

The synchrotron light source has the highest power and thus is suitable to obtain high quality CT images. X-rays with a desired energy level from the high-power synchrotron source can be obtained through a monochromator. A double-multilayer monochromator (DMM) and a double-crystal monochromator (DCM) are the two types of monochromators that are typically used in an optic hutch of synchrotron facilities. While the DCM delivers a highly monochromatic beam ($\Delta E/E \approx 10^{-4}$), the DMM provides an energetically broader beam ($\Delta E/E \approx 10^{-2}$), resulting in a much higher photon flux on the sample [20,21]. It allows fine quality X-ray images when the X-ray passes through the wide area. The Beamline 6C at Pohang Accelerator Laboratory (PAL) was equipped with the DMM and it was set to provide 27 keV X-rays for the present *in situ* testing.

Tension tests on the single edge notched specimens were performed using the *in situ* mechanical loading device. We have focused on the SENT test at PAL due to the limited beam time granted for the experiment. Figure 2-16(b) illustrates the *in situ* test setup with the X-ray beam path penetrating through the specimen mounted in the loading device. For the *in situ* mechanical testing, the first and the most important step is the beam alignment with the specimen region of interest (ROI). Figure 2-16(a) shows the precision rotation/translation stage that was used to align the X-ray beam path with the SENT specimen.

The beam alignment process began with mounting the loading frame onto the precision stage. Since the accurate height of the beam path was known, the z -direction positioning was first carried out. After the z -axis set up, the center of the path and the rotation axis of the loading device were aligned to reduce any potential noise factor during a reconstruction process. The rotation axis arrangement directly affects the quality of reconstructed 3D images. The arrangement was checked by comparing images taken at 0 and 90 degrees. The X-ray beam passed through the specimen was converted to visible light by the scintillator as illustrated in Figure 2-16(b). Scintillator materials absorb the energy of ionizing radiation and re-emit the absorbed energy in the form of visible light. PAL utilized a 100- μm thick CdWO₄ filter for the scintillation. Finally, the focusing process of the CCD camera was conducted. For the present experimentation, the distance from the sample to

the detector was set to 110 mm. The position of the focal point was decided on the desired magnification level. For the SENT test, we used 20 \times lens that resulted in the pixel size of 0.45 micro-meter per pixel with the field of view (FOV) being 1.8 mm by 1.2 mm, which is fine and large enough to observe the initiation and propagation of cracks near the notch tip. X-ray images were taken at the nine loading steps as indicated in Figure 2-17. Displacement-controlled loading was applied to the specimen and a specific displacement was maintained while X-ray images were being taken. At each of the nine steps, X-ray projection images were recorded at every 0.15° as the testing instrument was rotated stepwise through the total angular range of 180 degrees.

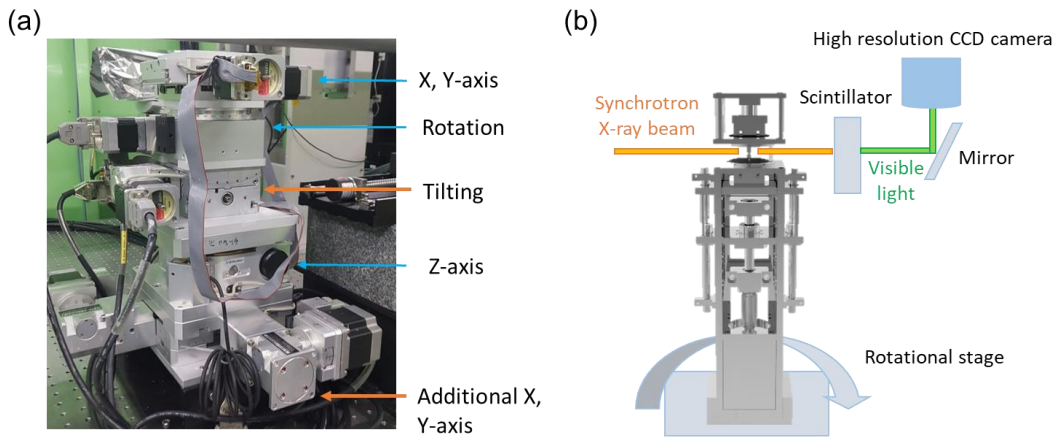


Figure 2-16: (a) Precision rotational/translational stages for the alignment of the specimen to the X-ray beam (b) Schematic illustration of the synchrotron X-ray beam system

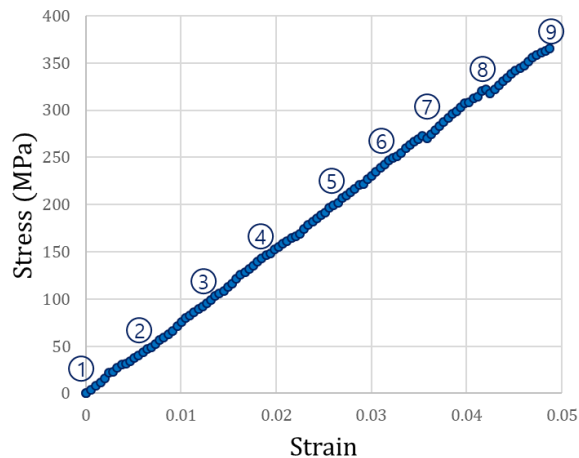


Figure 2-17: Stress-strain response of [90/0]S specimen with a single edge notch. Points 1 to 9 indicate the load when the X-ray images were taken.

Two dimensional (2D) tomographic slices (tomograms) of the specimen were first generated from the X-ray projection images (radiographs) using a commercial reconstruction algorithm, Octopus Reconstruction [23]. The solid materials (matrix and fiber) and vacancies (cracks, voids and air) had a different grayscale intensity representation. By segmenting the appropriate grey-scale values, cracks in the specimen could be identified. Figure 2-18 shows a tomogram of the SENT specimen reconstructed from the radiographs. As can be seen in the figure, the constituents of the specimen were represented with a high grey scale (white), while the cracks had a low grey scale (dark). Multiple failure modes were detected from the 2D tomographic slice image. Interfacial failure (delamination) was found at the interface between the 90° and 0° plies in the *xy*-plane 2D tomographic slice image. Fiber directional splitting in the 0° layer was also clearly visualized in the same *xy*-plane image. In addition, transverse matrix cracks in the 90° layers were observed in the *yz*-plane image. Comparing with the laboratory X-ray source, the fiber, matrix and crack were clearly distinguished owing to the high power of the X-ray source and finer resolution of the optic system at the synchrotron facility.

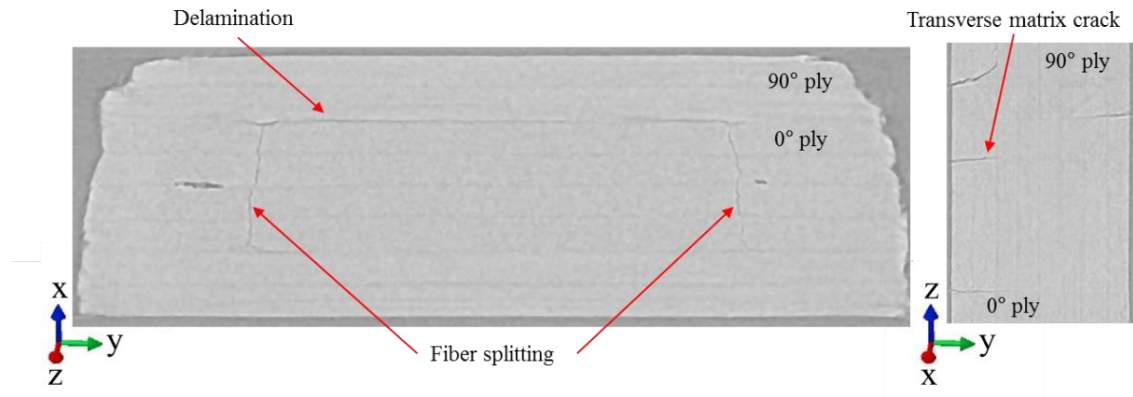


Figure 2-18: Example of 2D tomography slice images obtained from the in situ tensile test on [90₂/0₂]s specimen with a single edge notch. Multiple failure modes were detected.

3D volume images of the SENT specimen undergoing the mechanical loading were reconstructed from the tomograms using Amira Software 6.2 [24]. Computational tomography (CT) reconstruction allows the volume of a given sample to be visualized in a three-dimensional grey-scale map in which a specific grey-scale value is correlated with the X-ray absorption coefficient of a local material. The coefficient depends on the atomic

number and density of the local material. Figure 2-19 shows the reconstructed 3D volume image of the specimen before it was loaded. The 3D volume image was obtained at the notch tip with the ROI size being 1.13 mm thick, 2.4 mm high, and 2.8 mm wide.

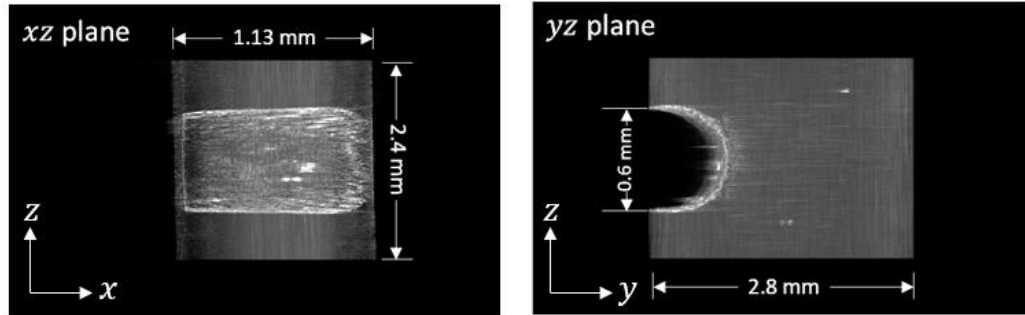


Figure 2-19: 3D volume image of the unloaded specimen near the notch tip

Figure 2-20 shows cracks displayed in the 3D volume image when the applied loads were at 35%, 45%, 57% and 68% of the failure load. Through the series of the volume images, the entire progress of various failure modes was observed. Transverse matrix cracks (red) in the 90° plies and the fiber directional splitting (blue) in the 0° plies occurred first near the notch tip as shown in Figure 2-20(a). Additional transverse cracks (yellow) in the 90° layers were found as the load increased as shown in Figure 2-20(c). It is interesting to note that the transverse matrix cracks in the 90° layers were initiated almost symmetrically with respect to the central plane at the notch tip. Delamination was also observed in the opposite side of the initial notch. As the load was increased, the transverse matrix cracks, splitting and delamination kept growing.

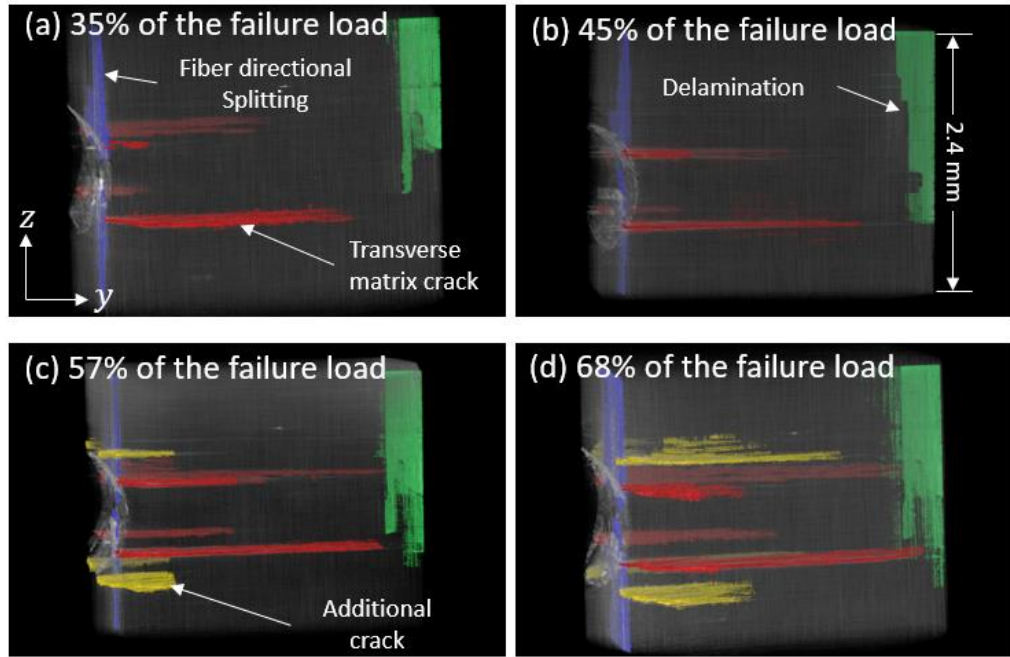


Figure 2-20: 3D volume image of the specimen with various failure modes at different loading steps

Figure 2-21 shows the same specimen in Figure 2-21, but from a different viewpoint. In order to clearly observe the fiber splitting mode, the 3D volume images were viewed in the xz -plane at the same loading steps used in Figure 2-21. As clearly depicted in Figure 2-20 and Figure 2-21, the failure modes were significantly dependent on the local microstructure of the laminated composite specimen, i.e., transverse cracks in the 90° layers and fiber splitting in the 0° layers.

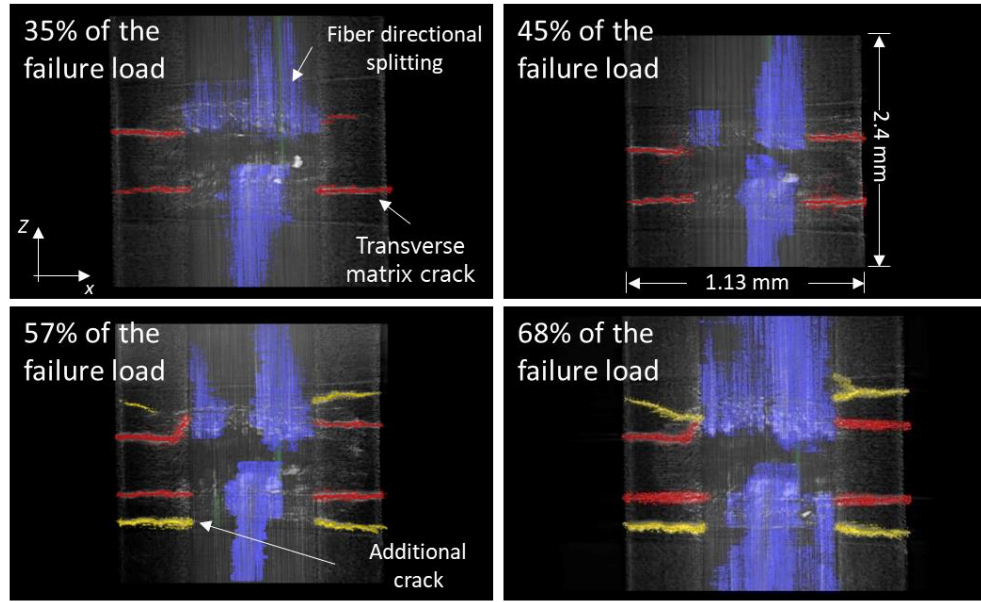
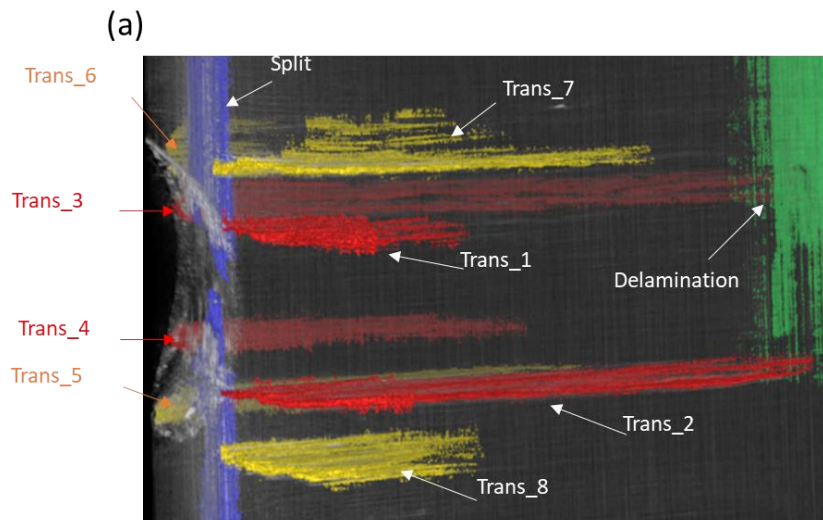


Figure 2-21: 3D volume images with the cracks viewed in the xz-plane

Figure 2-22(a) shows how the cracks were labeled and differently colored before the behavior of each crack was analyzed. The labeling and coloring were conducted using the Amira Software. After the cracks were classified according to their configurations and initiation sequences, each crack was named such as Trans_1, Trans_2, Delamination and so on as illustrated in Figure 2-22(a). For a clear distinction between the different fracture modes, each group of voxels for a specific cracking pattern had been painted with the same color. In this way, the quantification of the cracking behavior was easily conducted using the Amira Software.



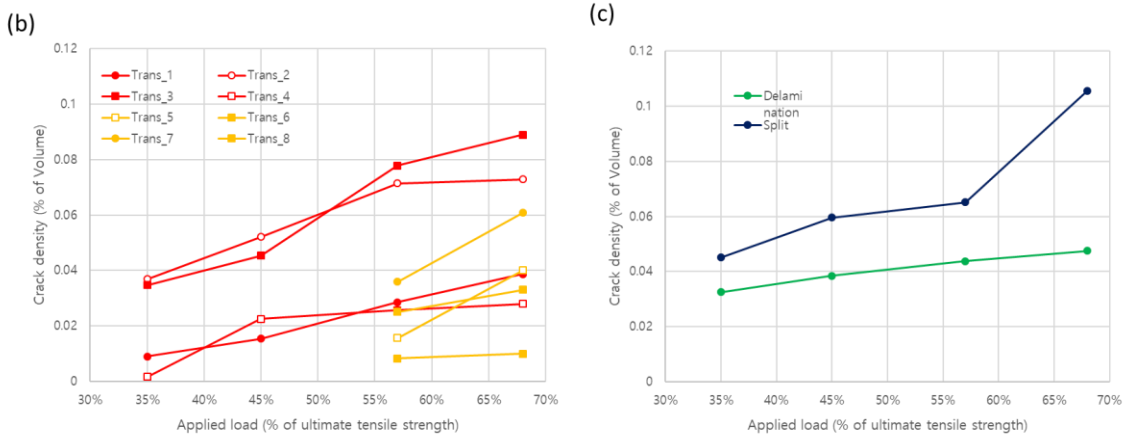


Figure 2-22: (a) Denotation of each crack (b) Growth of the densities of different transverse matrix cracks (c) Density changes for delamination and splitting failure

Through the volume images such as Figure 2-20 and Figure 2-21, the microstructural fracture behavior was quantitatively analyzed in terms of the crack density variance as the applied load increased. The crack density was measured from the volume of a crack divided by the initial volume of the specimen in FOV. The volume was measured by counting the number of voxels. In Figure 2-22(b) and (c), the colors of each curve are matched with the corresponding fracture modes displayed in Figure 2-22(a). In addition, the circle mark in Figure 2-22(b) indicate the cracks occurring in the left side of the 90° layers and the rectangular mark is used for the right side of the 90° layers. As shown in Figure 2-22(b), the densities of the initial transverse matrix cracks were increased as the applied load was increased. Additional transverse matrix cracks were initiated at 57% of the ultimate tensile strength and their densities rapidly grew. When the new cracks were propagated, the growth of the existing cracks were somewhat slowed down. The fiber directional splitting also suddenly propagated with the new transverse cracks while the delamination was constantly increased as the applied load was increased as shown in Figure 2-22(c).

CHAPTER 3: *In situ* thermomechanical tests on CMCs

3.1. Introduction

This chapter describes experimental tasks performed to observe subsurface behavior of ceramic matrix composites under combined thermal and mechanical loadings. Three major tasks were carried out and they are:

- Design and fabrication of an *in situ* thermal/mechanical loading device
- Thermal testing with X-ray tomography
- Thermomechanical testing with X-ray tomography

With the increasing demand of using advanced CMC materials for aerospace applications and gas turbines for power generation [22-27], it is crucial to have comprehensive knowledge of their thermomechanical performance at high temperatures. A keen understanding of the structural behavior of CMCs, especially at extremely high temperatures above 1200°C, is essential to maximize the benefits that the material can offer in high-temperature applications. Since the unique behavior of CMCs is attributed to their unique heterogeneous microstructure, it is desired to observe the microstructural behavior of the material subjected to thermomechanical loading. The X-ray tomography is a powerful visualization technique to obtain subsurface information of the material.

The aim of this chapter is to study *in situ* damage initiation and propagation in a CMC specimen subjected to a thermal and/or mechanical loading at a high temperature condition using X-ray tomography. A new loading frame with a heat chamber was required to observe thermomechanical microstructure behavior of the specimen. Many researchers have developed various heat chambers that can be used in conjunction with X-ray scanners. They can be distinguished based on heating types; resistance heating, gas flame heating, induction heating, and radiation heating systems. In the thesis, the radiation heating system consisting of four infrared halogen lamps was used. In the heat chamber, the lamps were placed such that a focal heat zone was constructed to effectively achieve a very high temperature at a spot of the specimen located in the zone [28-31]. Details of the device for the CMC materials will be provided in Chapter 3.2.

The loading device with the heat chamber was used to perform *in situ* thermal and/or mechanical tests on the CMC materials. First, thermal microstructural behavior of the specimen was observed at 900 and 1180 degrees Celsius using X-ray μ CT. Next, thermomechanical behavior of the material was examined with an increasing compressive load at 1200°C. Detailed observation results will be presented in Chapter 3.4.

3.2. Design and fabrication of a high temperature *in situ* device

3.2.1. Overview of the thermal/mechanical loading device

A loading device for performing *in situ* thermomechanical tests in the X-ray synchrotron beamline was designed and fabricated. The new loading device was equipped with the high temperature heating system. Since the *in situ* tests were performed at the same facility (Beamline 6C at PAL) for the experimentation described in Chapter 2, the same requirements and limitations on the weight (maximum 20 kg) were applied to the thermomechanical loading device even with the heating chamber.

In the design process, the components of the loading frame were divided into two categories; direct loading subassembly and structural supporting subassembly. Parts in the direct loading unit transfer a load from a mechanical energy source to a specimen and thus should be strong enough to sustain the applied load when it is being conveyed. All the components in the direct loading system were manufactured using the SUS304 material. However, the steel material is very heavy, the structural supporting unit was made of aluminum to reduce the overall weight of the loading frame. In addition, all the components were designed in an axisymmetric shape to minimize the rotary inertial effect on the precision rotation stage. Details about the loading and structural units are described in Chapters 3.2.2.

The heating system was required to heat up the specimen over 1200°C, which is a typical operating condition of a hot section in a gas turbine engine. A specimen was mounted in the center of the chamber that was installed above the mechanical loading system. The heating system was composed of four 150W infrared halogen lamps, which was operated by a programmable power supply. An inspection window with sapphire glass (CaF_2) was designed to measure temperature of the specimen surface with a pyrometer. In

order to protect the mechanical loading system from being damaged due to the high temperature, insulating layers were placed in both top and bottom sides of the chamber. The insulating layers prevented heat from being transferred to the loading system and protected important yet weak components in high temperatures such as the load cell and the linear bush. Ceramic material was used for the layers owing to its low thermal conductivity. Details about the heating system will be presented in Chapter 3.2.3. Figure 3-1 shows the *in situ* thermomechanical loading frame mounted on the testbed at PAL.

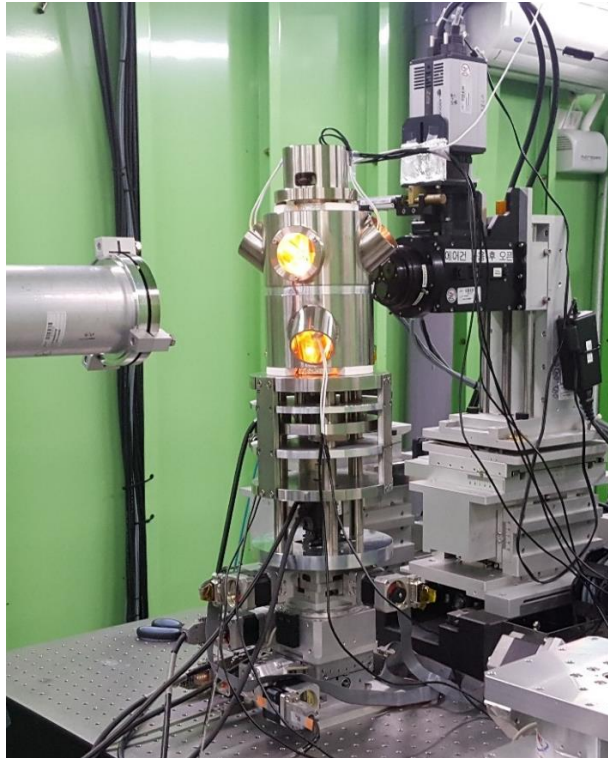


Figure 3-1: *In situ* thermomechanical loading frame installed in PAL

In the previous loading device, the specimen was surrounded by a polymethyl methacrylate (PMMA) tube which is transparent and has a low density. However, PMMA is not a suitable material in a high-temperature environment. For the thermomechanical loading frame, the temperature of the surrounding tube was expected to reach over 200°C during the thermal loading tests running at 1200°C. A very thin aluminum alloy (Al-Mg-Si alloy 6061-T6) was found to be a best solution for the surrounding tube. Based on the previous calibration results on the transmission efficiency of X-ray energy for aluminum [32], the tube thickness was selected such that it is thick enough to withstand the

mechanical load and thin enough not to deteriorate the transmitted X-ray beam too much before it reaches to the specimen. The tube had the thickness of 300 μm , the height of 10 mm and the diameter of 140 mm. When the X-ray beam passes through the aluminum tube with the thickness of 300 μm , the transmission rate is over 80% [33], which is enough to obtain clear projection images.

3.2.2. Mechanical loading system

The loading system as shown in Figure 3-2 was designed and fabricated to apply an axial load of up to 1 kN to a CMC specimen. From typical strengths of CMC materials reported in literature [34], the maximum load capacity was determined to investigate pre-peak as well as post-peak response of the material from *in situ* thermal/ mechanical tests. The operation principle of the loading system was similar to the previous loading frame presented in Chapter 2.2.2. Torque generated from a stepper motor was converted to an axial load through a linear actuator system with a ball screw as illustrated in Figure 3-2. The required torque from the stepper motor to achieve the desired load capacity was calculated from Eq. (2-1) and it was found to be 0.35 N·m. The selected stepper motor (MR-J4-KR-13, Mitsubishi Corp. [16]) has a rated torque of 0.35 N·m. In addition to the capacity, the weight and height of the motor were also considered because of the precision rotational stage at PAL. The selected stepper motor was 76 mm high and its weight was 0.54 kg.

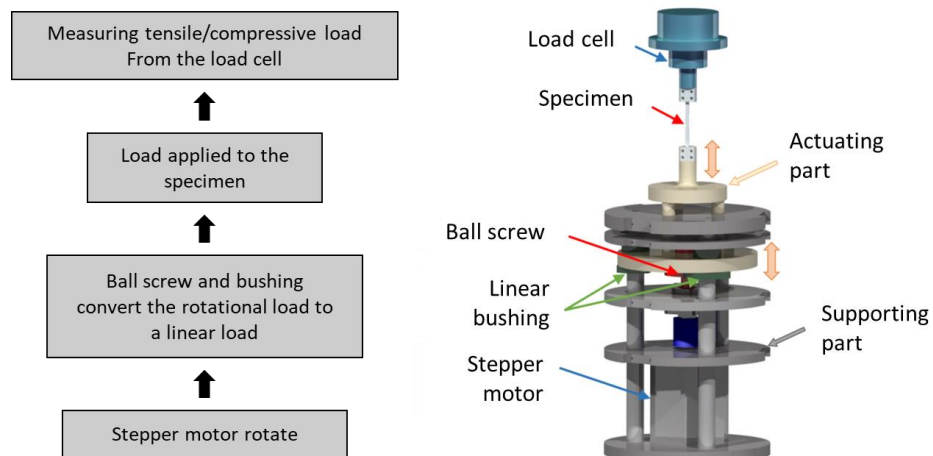


Figure 3-2: Schematic of the operation principle of the specimen loading system

3.2.3. Thermal loading system

In the previous loading device, the X-ray penetration window was fabricated with a PMMA material. However, for the thermomechanical testing, the penetration window was expected to be heated up to 80°C during the test. Hence, a very thin aluminum alloy was used for the window. Figure 3-3 shows the transmission rate as a function of X-ray energy for various aluminum thicknesses [33]. As can be seen in Figure 3-3, the transmission rate is about 80% at 25 keV when the aluminum thickness is 600 µm. For the thermomechanical testing at PAL, 25 keV photon energy was used for the CMC specimen. It was concluded that half of the 600 µm would be good enough for the window thickness since the X-rays would penetrate the window twice before they were collected from the detector. 300 µm thickness was thin enough not to deteriorate the transmitted X-ray beam and thick enough to withstand the mechanical load.

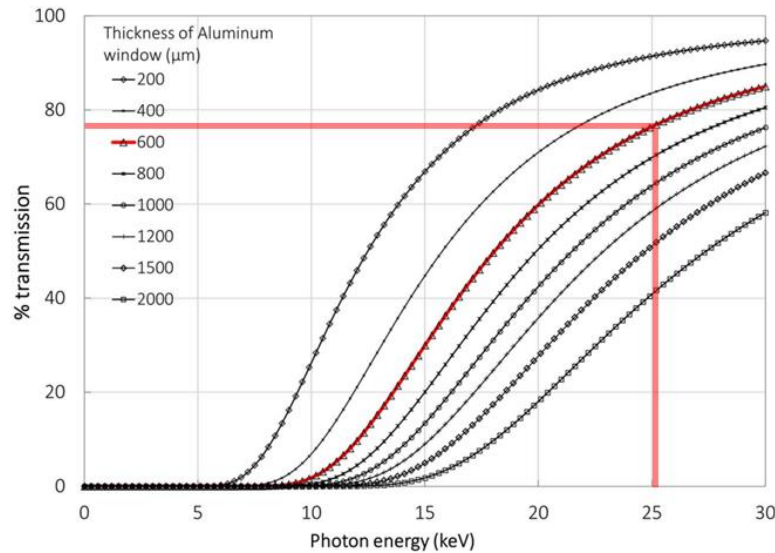


Figure 3-3: Transmission rate as a function of X-ray energy for various path length through an aluminum window [33]

The capacity of the heat chamber is greatly influenced by the number of heat sources, the total power of the heat source and the desired size of a hot zone. The present thermal loading device implemented four 150-Watt infrared halogen lamps fitted with gold ellipsoidal reflectors (L6409, 25V, 150W, focal length of 44 mm, International Light Technologies, Inc. [35]) as shown in Figure 3-4. The gold ellipsoidal reflectors provided

good infrared reflectance and light focusing. The lamps were installed to heat up a local region of the specimen from four directions in the confocal geometry. The positions of each halogen lamps were selected to establish a focal heat zone in the center of the chamber where the X-ray beam passed as shown in Figure 3-5. The specific positions of the four lamps formed the focused heat zone in a spherical shape with the diameter of 2 mm. The lamps were operated and controlled by a programmable power supply (ZUP40, 840 W, TDK-Lambda Inc. [36]). The temperature in the focal heat zone was adjusted by changing the output of the power supply. This radiation heating system facilitated a compact sized chamber suitable for the limited space in the beamline due to the short distance between the X-ray source and the detector.

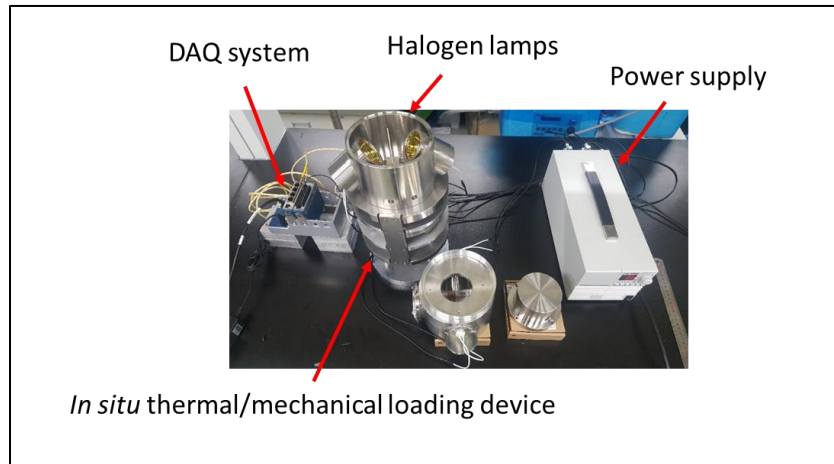


Figure 3-4: Components of the heating chamber

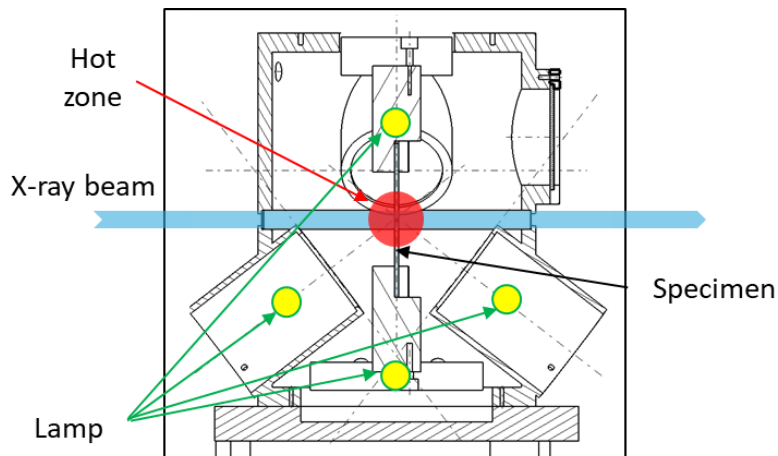


Figure 3-5: Focal heat zone at the center of heat chamber with four lamps

Before conducting *in situ* thermomechanical tests, the performance of the radiation heating system was evaluated. The temperature in the heating zone was measured with a ceramic beaded B type thermocouple (B type thermocouple Pt30% Rh, 204~1700°C, Omega engineering Inc. [37]) as shown in Figure 3-6(a). The tip of the thermocouple was located in the heating zone and the ceramic tube insulating the thermocouple was held by the bottom grip of the loading device. A data acquisition system (NI-9211, National Instruments Corp. [17]) managed through the LabView platform [18] was used to measure the temperature. Figure 3-6(b) shows temperature measurements at various input powers. Since the heat chamber had four 150-Watt halogen lamps, the maximum input power for the evaluation was slightly less than 600 Watts. As can be seen in Figure 3-6(b), the heating rates from the room temperature to peak temperatures were very rapid in all the tests. It took less than one minute to reach the peak temperatures, which were correspondent with each input power indicated in Figure 3-6(b). At the peak temperatures, they remained stable for a long time as depicted in Figure 3-6(b). Temperature stability was crucial for successful *in situ* tests since X-ray scanning typically takes more than half an hour. Note that, at the input power of 582 W, the peak temperature was measured to be 1175°C. Since the temperature was recorded when the chamber was not closed, there might be some temperature loss. However, 1175°C was close enough to the target temperature, 1200°C, even at the input power less than the maximum power.

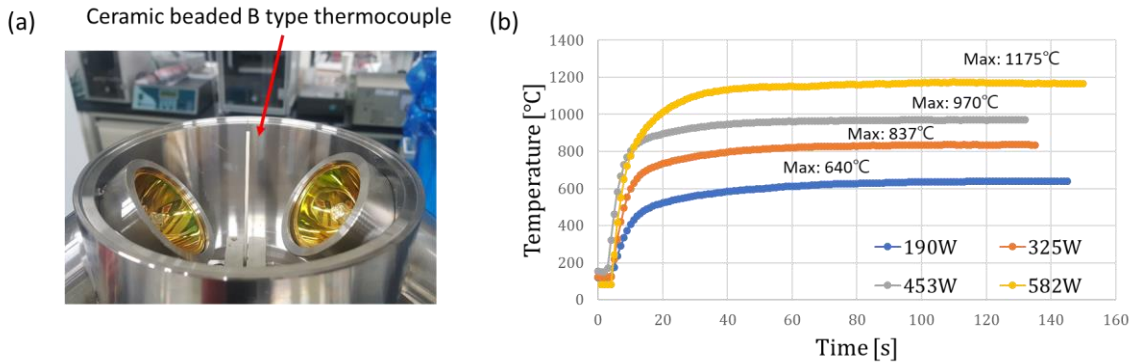


Figure 3-6: Temperature measurement in the heat zone (a) Ceramic beaded B type thermocouple (b) Peak temperatures with a variance of input powers

Next the temperature on the specimen surface in the heat zone was measured using a pyrometer (IGA 6 Advanced, 250~1800°C, Luma Sense Technologies Inc. [39]) as shown

in Figure 3-7. Pyrometry technique that measures the temperature from an emitted thermal radiation is a very accurate remote measurement method for the surface temperature of a specimen [33]. Especially in the high temperature condition, it is a convenient approach and more accurate than a conventional thermocouple. However, the present heating system may result in erroneous measurements due to the radiation directly coming out from the heat sources, not from the specimen. Hence, in the present heat chapter, a sapphire glass window was installed to measure the specimen temperature using a pyrometer. CaF₂ material can filter the radiation emitted from the halogen lamps as well as transmit the significant radiation that is used to measure the temperature by the pyrometer. Figure 3-8 shows temperature measurements on the specimen as the total input power was changed. Peak temperatures were recorded after they were sufficiently stabilized as shown in Figure 3-6(b). The results in Figure 3-8 was utilized as a calibration data in controlling the temperature on the specimen by the input power. Figure 3-9 shows the temperature stability test results conducted at the maximum input power condition. With the system running continuously over a 2-hour period, the specimen temperature remained almost constant at the maximum temperature as shown in Figure 3-9.

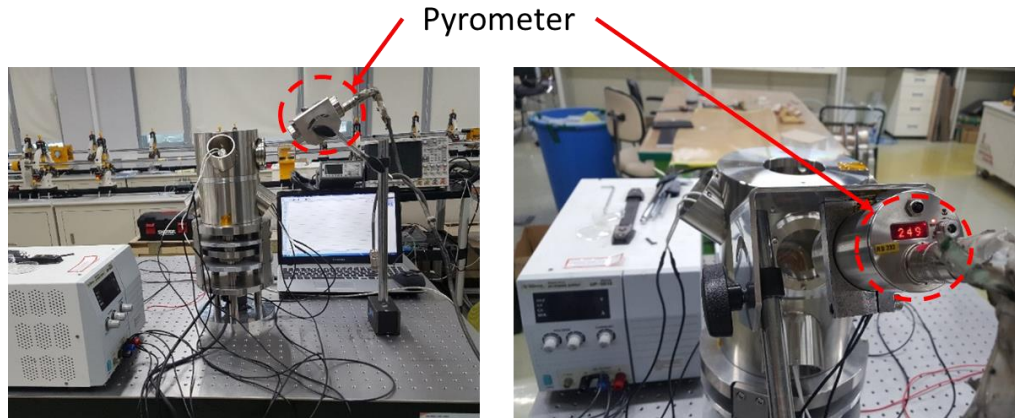


Figure 3-7: Pyrometer set up for measuring the temperature of a specimen

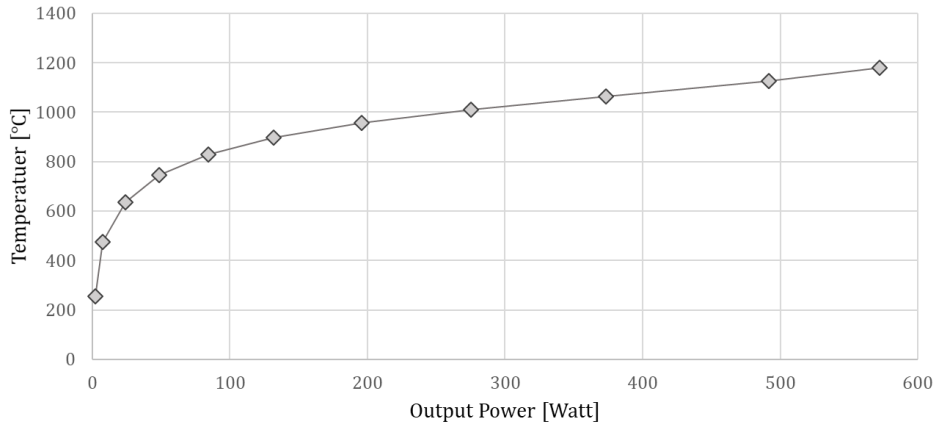


Figure 3-8: Temperaure easured by pyrometer as a function of power supplied to heating lamps

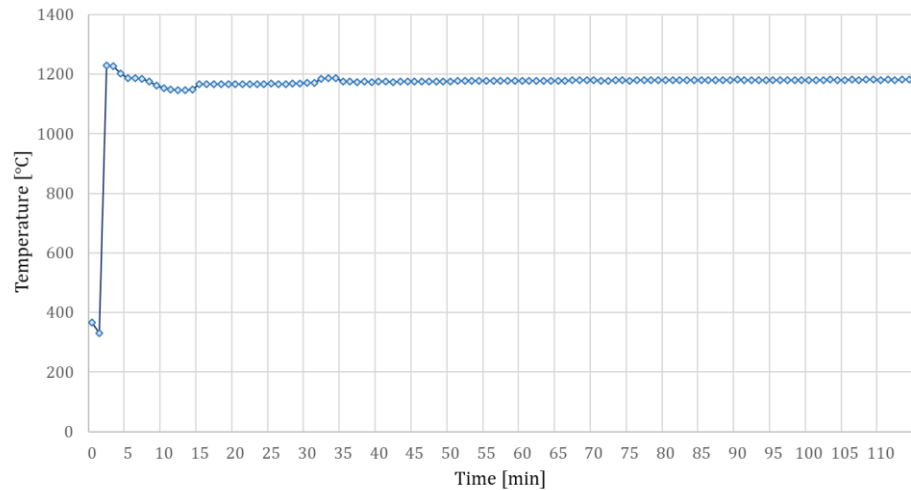


Figure 3-9: Temperature continuity test result over a 2h period

3.2.4. Specimen grip system

Figure 3-10 shows grips that hold a specimen in the thermomechanical loading device. In the mechanical loading tests, one of the typical errors are specimen slipping in the grips. CMC specimens have an extremely high surface hardness. In the *in situ* loading device, specimen holding system was designed to provide a non-slip condition. As shown in Figure 3-10, four M3 bolts were used to tightly grasp the specimen. One side of the specimen was mounted in the center of the grip and pressed by bolts from both sides. In addition, the grips were made of a material that is durable at such a high temperature without melting or

expanding. Invar 36 has an extremely low thermal expansion coefficient (1.30×10^{-6} cm/cm/ $^{\circ}$ C) and thermal conductivity (10.5 W/m·K).

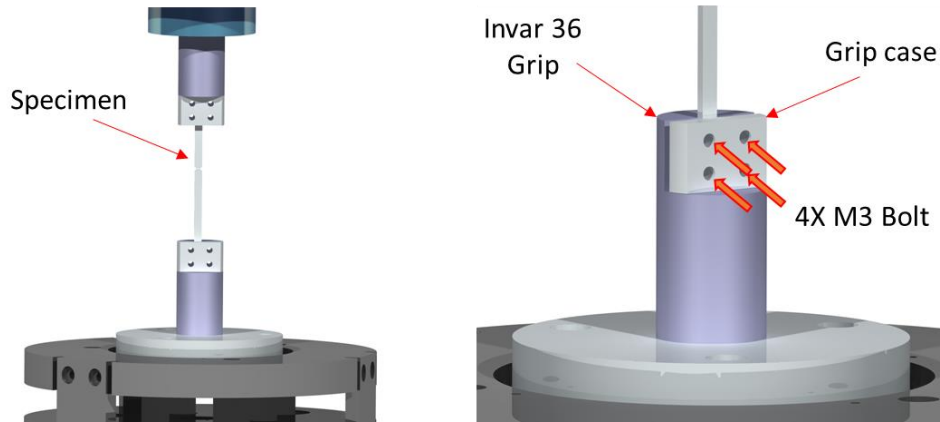


Figure 3-10: Specimen holding system with Invar 36

3.3. CMC specimens

3.3.1. Examination of the specimen

CMC specimens were provided from DACC Carbon Company. Before performing *in situ* tests, SEM and μ CT analyses were conducted to examine the internal microstructure of the specimens. Figure 3-11(a) shows an internal microstructure of a CMC sample reported in [39] and Figure 3-11(b) shows the internal structure of the DACC CMC specimen. The DACC specimen was composed of SiC fibers, SiC matrix and carbon matrix. Ceramic fiber layers were filled with ceramic and carbon matrix. Also, μ CT scan is a useful method to observe the complex subsurface structure, which can give an insight to the potential microstructural behavior of the CMC specimens. A series of CT scanning was conducted with the in-house μ CT scanner (Skyscan1176, Brucker Inc. [39]). Figure 3-12(a) shows the typical microstructure of the CMC specimen in three-dimensional space. In the image, the ceramic layers and ceramic matrix could not be fully distinguished because they have same intensity level. Only the carbon matrix between the ceramic layers was observed. Figure 3-12(b) shows a 2D tomographic image of the specimen. The ceramic matrix was formed between the fiber layers like a honeycomb structure. This implies that the matrix has not been sufficiently infiltrated between the fiber layers during a manufacturing process. The coarse internal structure may cause failure at a lower stress than its expected strength.

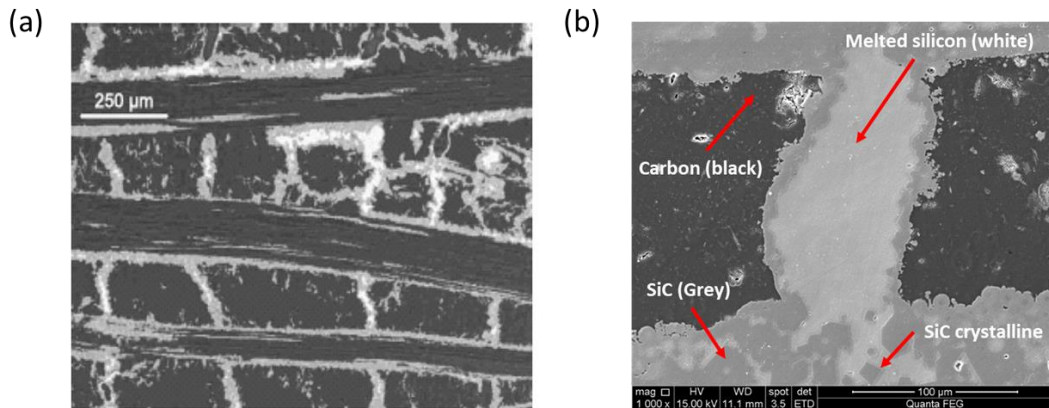


Figure 3-11 (a) C/C-SiC: C/C segments (darks), SiC (grey) and silicon (white) [39] **(b)** SEM result of the present CMC specimen

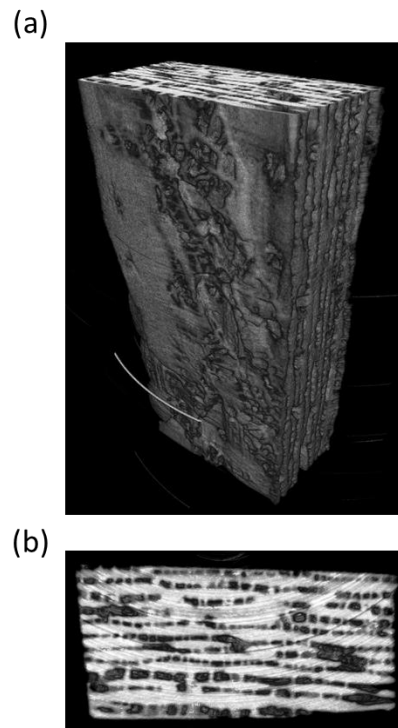


Figure 3-12: Microstructure of a CMC specimen (a) three-dimensional (b) viewed in the xy plane

3.3.2. Specimen fabrication for in situ tests

Conventional machining and water-jet cutting were not applicable in fabricating CMC specimens due to the high strength and hardness of the material. A low speed sawing machine (Low speed precision cutter, Buehler Inc. [41]) with a diamond cutting blade was

suitable for cutting a material with a high hardness. When fabricating a test coupon, the specimen was pushed downward with a small force, using its own weights and a pendulum as shown in Figure 3-13. Many attempts were made to find an optimized machining condition for the CMC coupon. In addition, a liquid-type coolant was constantly provided to prevent the coupon from being over-heated during the machining and to enhance the quality of the cutting surface. The optimized processing speed for cutting the CMC coupon was about 10 mm per 4 hours. It took 16 hours to fabricate a bar-shaped specimen with a dimension of 62 mm × 4 mm × 2.5 mm.

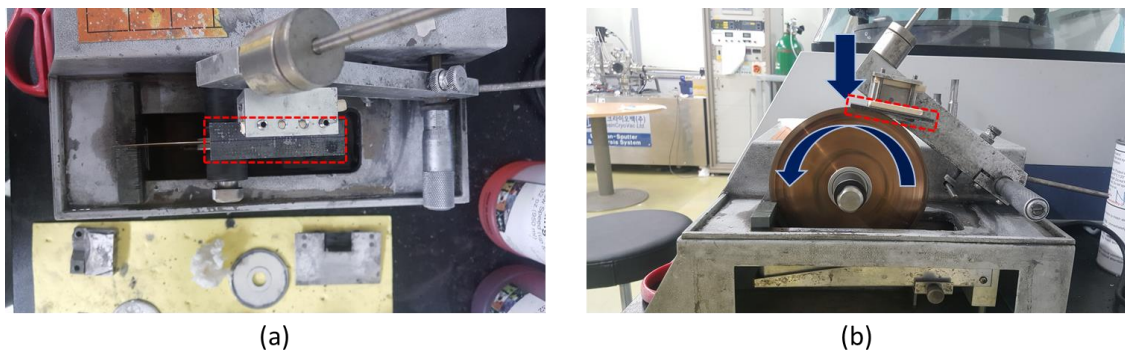


Figure 3-13: Specimen fabrication with a low-speed diamond saw

3.4. Thermal/mechanical tests with X-ray synchrotron

3.4.1. In situ thermal loading test

The thermal characteristics of the CMC material were investigated with X-ray micro tomography technique. The experiments were conducted using the thermomechanical loading device in Pohang Accelerator Laboratory (PAL). In the *in situ* thermal loading tests, as shown in Figure 3-14, the top side of the specimen was not fixed and thus a mechanical load was not applied to the CMC specimen when the thermal load was applied. X-ray scanning was conducted at three different steps, room temperature, 900°C and 1200°C, to observe the thermal response of the CMC microstructure. A set of X-ray projection images (radiographs) consisting of 600 radiographs was obtained at each scanning sequence, which typically took an hour.

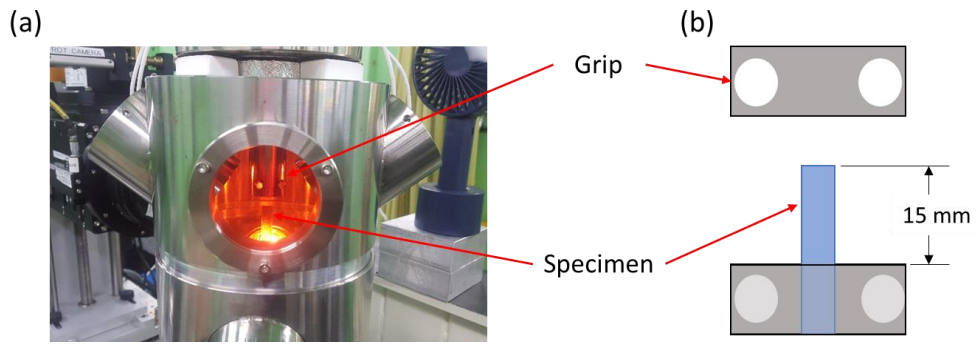


Figure 3-14: Specimen installation for *in situ* thermal loading test

Figure 3-15(a), (b) and (c) are the 2D slice images that show the microstructure of the CMC specimen at 25°C, 900°C and 1200°C, respectively. Through the series of the tomography images, the thermal characteristics of the CMC specimen were investigated. In the 2D slice image at 25°C, no clear distinction between fiber and matrix regions was identified. Instead, it was found that the CMC specimen was filled with two constituents. Different materials have different X-ray transmission rates and they appear as different intensities in the images. The bright color which had a more absorption rate was estimated as a ceramic material. However, the other phase, which was shown in darker color, filled the specimen. As the temperature increased to 900°C, no significant deformation of the microstructure was observed in Figure 3-15(b). At 1200°C, as shown in Figure 3-15(c), image quality was very poor. The main reason of the poor quality may be due to the constant thermal deformation of the specimen during X-ray scanning which can cause an error during a reconstruction process.

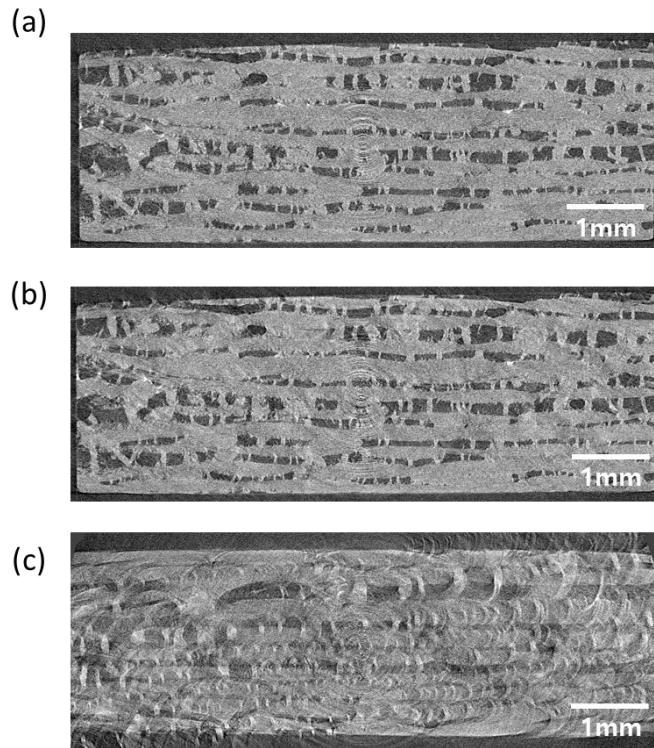


Figure 3-15: 2D slice images and 3D CT results from *in situ* thermal tests

In the *in situ* thermal test, any significant deformation of the internal structure was not observed. Figure 3-16(a) shows the matrix layer that looks like a fishing net. It is hard to observe the thermal characteristics because of the complex inner structure of the CMC specimen. Figure 3-16(b) and (c) shows that there exists a debris inside the specimen. Although the type of the material cannot be verified, the material in the middle of the specimen had a low X-ray absorption rate and it appears in a very bright color. Since it was difficult to identify specific structural features within the CMC specimen, the debris that had a particular shape and location was used as a major landmark in observing any changes in the material. By measuring the displacement and volume changes of the debris, the thermal behavior of the CMC specimen was indirectly examined. Location changes of the debris in the longitudinal direction was measured at each temperature stage. When the specimen was heated from room temperature (25°C) to 900°C , the debris vertically moved by $46.2 \mu\text{m}$. Next, the debris moved by $191.4 \mu\text{m}$ when the specimen was heated up to 1200°C . Based on the position changes of the foreign object, it can be concluded that the CMC specimen was thermally expanded during the *in situ* thermal tests since the CMC

specimen had the same displacement with the debris. Thermal expansion of the specimen can be calculated from

$$\varepsilon = \alpha \Delta T \quad (3-1)$$

$$l = \varepsilon \times l_0 \quad (3-2)$$

where α is the thermal expansion coefficient ($4.3 \times 10^{-6} \text{ } 1/\text{ } ^\circ\text{C}$), ΔT is the change in temperature, l_0 is the initial length. When the specimen was heated from room temperature to 900°C , the extension is computed to be $56.3 \mu\text{m}$, which is a close to the measured change from the X-ray tomography images.

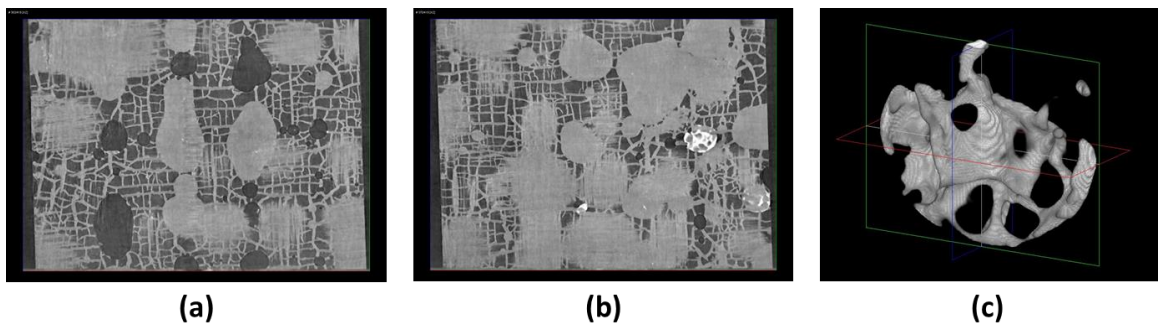


Figure 3-16: (a) Fishnet-shape matrix (b) Debris found in the specimen (c) Debris in 3D space

3.4.2. *In situ* thermomechanical loading test

Thermomechanical behavior of the CMC specimen was investigated with X-ray tomography. Figure 3-17 shows the specimen mounted in the loading device. The bottom part was fixed by the grip and the compressive load was applied using a steel block at the other side. A piezo-electric type load cell measured the compressive load applied to the specimen. After mounting the specimen, the temperature was set to 1200°C . First X-ray scan was conducted at 1200°C without any compression. For the next steps, X-ray scans were carried out at compressive loads of 200 N and 910 N.

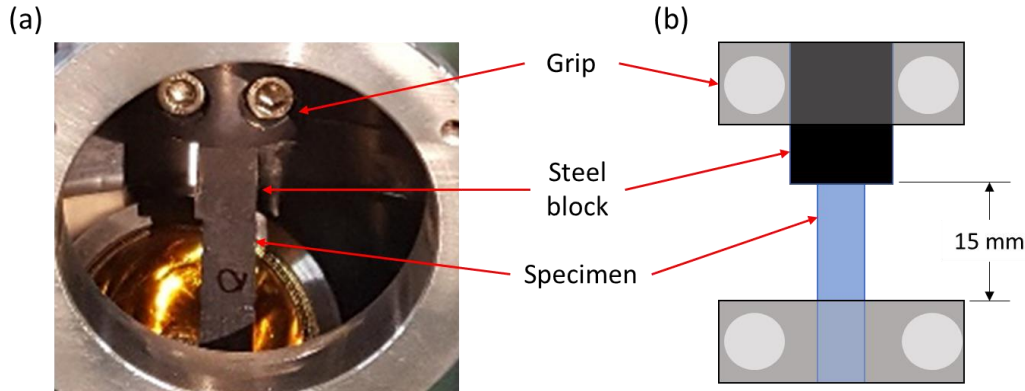


Figure 3-17: Specimen loading for *in situ* thermal/mechanical loading test

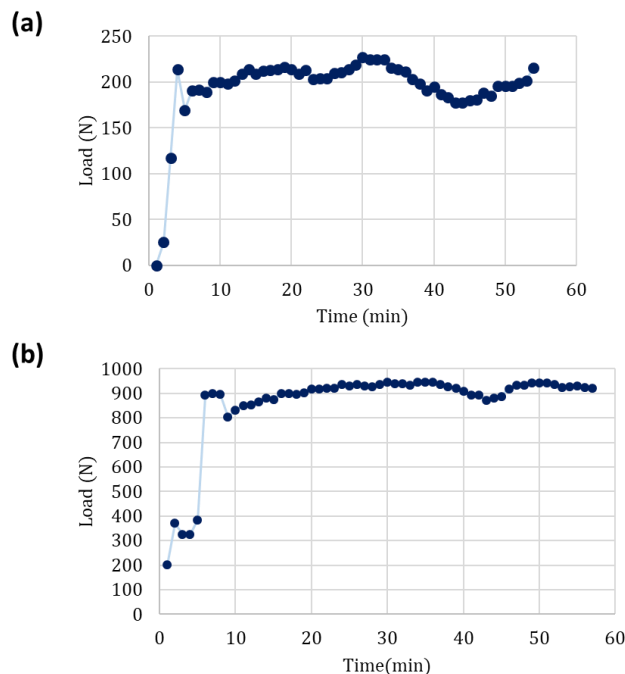


Figure 3-18 Measured compressive load during X-ray scanning (a) 200N (b) 910N

Figure 3-18 shows the recorded compressive load that was being applied to the CMC specimen during the X-ray scanning. The load graph shows no significant changes in the compressive load and it can be concluded that the applied load remained reasonably constant when the X-ray scanning was being performed. The slight change in the load data was insignificant while the specimen was being rotated for the X-ray scan.

Figure 3-19 shows the results of the X-ray tomography results at 1200°C with a variance of the compressive load. Figure 3-19(a), (b) and (c) correspond to the load of 0 N,

200 N and 910 N, respectively. When the load was at 0 N, the image quality was also poor as in the case of the thermal loading test. However, it was found that the quality of the slice images at the same temperature (1200°C) was much more improved when the load was present. In the thermomechanical testing, the CMC specimen was fixed by the compressive load during the X-ray scanning. The image quality loss could be reduced since the specimen would not move while the loading was being applied unlike the case of the thermal loading test in which one side of the specimen was free to move. As the compressive load increased from 200 N to 910 N, the quality of the X-ray tomography results was gradually improved as can be seen in Figure 3-19(b) and (c). However, again, no significant deformation of the internal structure was observed even with the applied loads from the tomographic images.

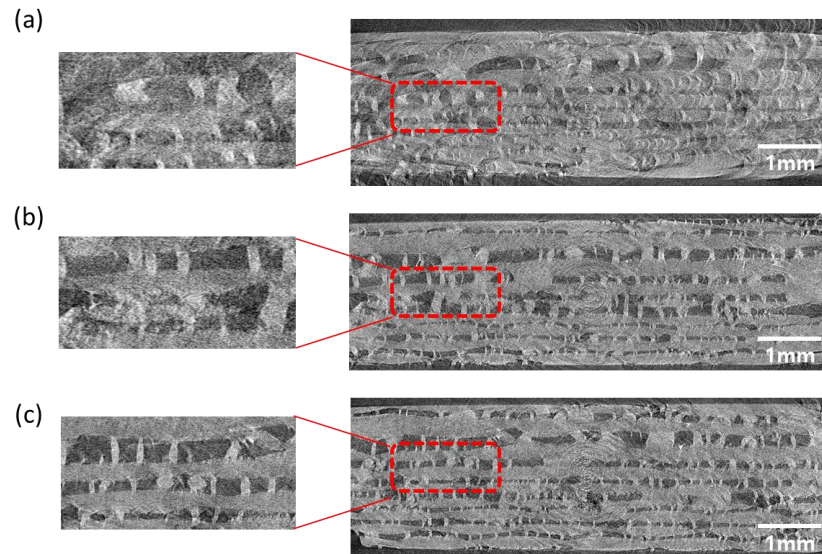


Figure 3-19: Fully 3D tomography results of *in situ* thermal/mechanical loading test

The thermomechanical behavior of the specimen was further investigated by analyzing the two-dimensional tomographic images. It was difficult to identify the internal structure from the images obtained at the first step of the X-ray scanning because of the image quality loss. Results of the compressive loads of 200 N and 910 N were used to study the microstructural behavior of the specimen. Two different characteristic images were selected from 2D tomography results when the specimen was loaded by 200 N. Then, the new locations of the images were found in the results when the specimen was compressed

by 910 N. Distinctive features of the inner structure were used to correlate the images between the different loading steps. Displacement and strains were calculated from the location information of the characteristic images between 200 N and 910 N. Figure 3-20 schematically illustrate the aforementioned correlation process. It was found that the specimen was moved 2.3 mm during the compressive loading. However, due to the potential compliance issue of the *in situ* loading device, the measured displacement may not be interpreted as the pure deformation of the CMC specimen. In other hand, the strain of the specimen had been measured accurately in the experiment. The distance between the two images was kept constant even after the load was increased. This result implies the absence of any deformation inside the CMC specimen while the compressive load was applied in the high temperature condition.

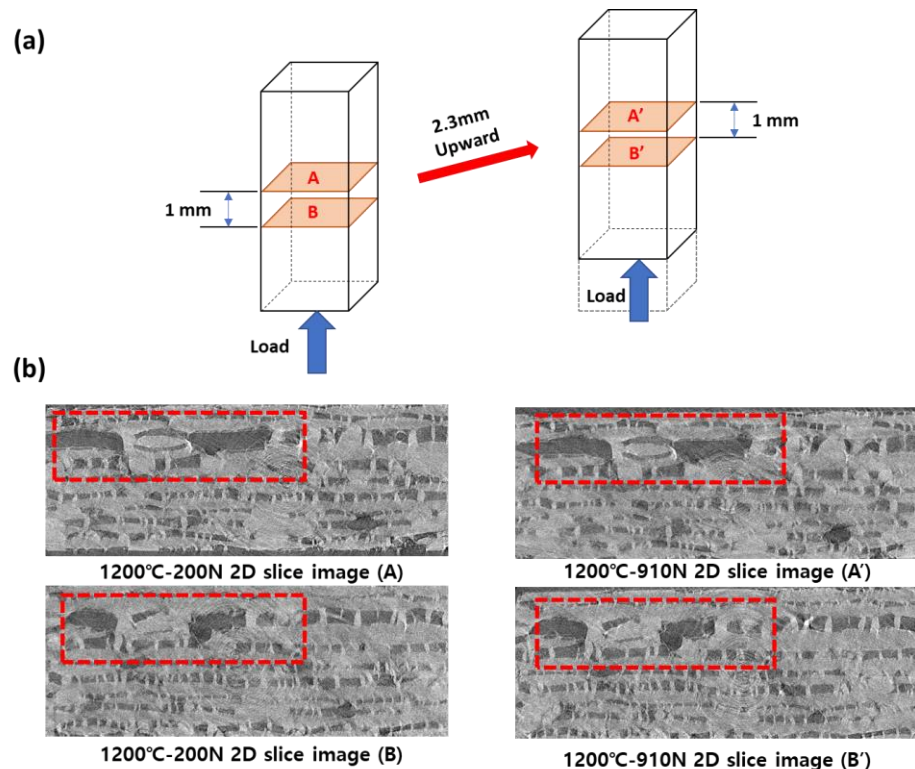


Figure 3-20: 2D slice images result of the *in situ* thermal/mechanical tests (a) specimen movement (b) selected characteristic images

CHAPTER 4: Conclusion

4.1. Conclusion

The present study utilizes various approaches including fabricating the *in situ* thermal/mechanical loading frame and *in situ* testing with X-ray tomography to investigate the structural behavior of the composite materials. *In situ* loading device has been designed and manufactured that is installed in the X-ray tomography beamline (Beamline 6C) at PAL.

In situ mechanical test results on the fiber-reinforced polymers with the layup sequence of [90₂/0₂]_s and [45₂–45₂]_s have been presented. Custom-built loading frame is designed and fabricated to perform the *in situ* tests. The loading frame is designed such that it can be mounted on the test stage at the synchrotron facility and X-ray images can be taken at certain loading steps. Reconstructed 3D tomography images clearly visualize multiple failure modes occurring at the different loading steps. Interactive failure mechanisms inside the heterogenous composite material is quantified using densities of each failure mode computed from image processing.

In situ thermal and mechanical test results on the ceramic matrix composites have been presented. The thermal/mechanical loading frame is designed and fabricated to perform the *in situ* test with X-ray tomography. The loading frame is designed such that it can heat up a specimen up to 1200°C with four infrared halogen lamps. Thermal behavior of the CMC specimen is examined at the different temperature steps. The structural behavior of the specimen which is applied the compressive load at high temperature is observed.

4.2. Novelty and contribution

The present study is concerned with unique testing and visualization techniques to characterize complex and interacting failure modes observed in composite materials under thermal and mechanical loading. Three-dimensional (3D) X-ray tomography microtomography (μ CT) has been utilized to visualize microstructural behavior in composite materials. *In situ* thermal/mechanical loading device is designed and fabricated that is installed in the synchrotron. Initiation and propagation of the subsurface failure in the composite materials are visualized. Interactive failure mechanism, due to the unique

microstructure of the composite materials, is investigated. Fully 3D computed tomography technique gives more information and insight for composite materials.

4.3. Future works

Although many researches have been performed to characterize damage and failure at the micro-length scale, they rely on hypothetical theories based on the observation of failure patterns from tested specimens. In the present *in situ* mechanical loading tests on the fiber-reinforced polymers have been investigated the initiation and propagation of various inner failure with X-ray tomography. Also, multiple failure modes and their interactions on the subsurface of the specimen are observed and quantified in the tests, as shown in Chapter 2.4.3. Based on the *in situ* tests results, micro-scale model shall be developed to predict and characterize the subsurface behaviors of composite materials.

Two types of the *in situ* loading devices have been designed and manufactured. However, the structural lack of the loading frame produces an inaccurate experiment result, especially in strain data during mechanical test. It means that the loading frame is deformed when the load is applied to the specimen. For the reliable test result, structural loading parts shall be revised and modified to withstand the applied load without any deformation. So, the *in situ* loading devices shall be revised to improve compliance issues.

Ceramic matrix composites are being developed because of the high service temperature over 1500 degree Celsius. However, as shown in Chapter 3, the maximum temperature of the designed and fabricated *in situ* thermomechanical loading device is just 1200 degree Celsius. Therefore, to characterize the thermomechanical properties in service temperature, heat chamber system shall be revised to reach the higher temperature environment.

REFERENCES

- [1] Jones, R.M., (1999). *Mechanics of Composite Materials*, Taylor and Francis, Philadelphia, PA.
- [2] Stock, S.R., (2008). “Recent advances in X-ray microtomography applied to materials,” *International Materials Reviews*, **53**, 129-181.
- [3] Sakdinawat, A. and Attwood, D., (2010). “Nanoscale X-ray imaging,” *Nature Photon* **4**, 840-848.
- [4] Buffiere, J.Y., Maire, E., Adrien, J., Masse, J.P. and Boller, E., (2010). “In situ experiments with X ray tomography: an attractive tool for experimental mechanics,” *Experimental Mechanics*, **50**(3), 289-305.
- [5] Moffat, A. J., Wright, P., Helfen, L., Baumbach, T., Johnson, G., Spearing, S.M. and Sinclair, I., (2010). “In situ synchrotron computed laminography of damage in carbon fibre-epoxy [90/0]s laminates,” *Scripta Materialia*, **62**(2), 97-100.
- [6] Wright, P., Moffat, A., Sinclair, I. and Spearing, S.M., (2010). “High resolution tomographic imaging and modelling of notch tip damage in a laminated composite,” *Composites Science and Technology*, **70**(10), 1444-1452.
- [7] Scott, A.E., Mavrogordato, M., Wright, P., Sinclair, I. and Spearing, S.M., (2011). “In situ fibre fracture measurement in carbon-epoxy laminates using high resolution computed tomography,” *Composites Science and Technology*, **71**(12), 1471-1477.
- [8] Garcea, S.C., Mavrogordato, M.N., Scott, A.E., Sinclair, I. and Spearing, S.M., (2014). “Fatigue micro mechanism characterization in carbon fibre reinforced polymers using synchrotron radiation computed tomography,” *Composites Science and Technology*, **99**, 23-30.
- [9] Hufenbach, W., Bohm, R., Gude, M., Berthel, M., Hornig, A., Rucevskis, S. and Andrich, M., (2012). “A test device for damage characterization of composites based

- on in situ computed tomography,” *Composites Science and Technology*, **72**(12), 1361-1367.
- [10] Bale, H.A., Haboub, A., Macdowell, A.A., Nasiatka, J.R., Parkinson, D.Y., Cox, B.N., Marshall, D.B. and Ritchie, R.O., (2013). “Real-time quantitative imaging of failure events in materials under load at temperatures above 1600 degrees C,” *Nature Materials*, **12**(1), 40-46.
- [11] Sket, F., Rodriguez-Hortalal, M., Molina-Aldareguia, J.M., Liorca, J., Maire, E. and Requena, G., (2015). “In situ tomographic investigation of damage development in +/- 45degree carbon fibre reinforced laminates,” *Materials Science and Technology*, **31**(5), 587-593.
- [12] PAL, <http://pal.postech.ac.kr/paleng/b1/6c>.
- [13] KIST, <http://eng-jb.kist.re.kr/business/en/index.do>.
- [14] XHUBER, “Positioning devices-rotation-1 circle-Goniometer 409,” www.xhuber.de/en/product-groups/1-positioning-devices/12-rotation/1-circle-goniometers/409/, Accessed November 23, 2017.
- [15] Honeywell, “Sensing and internet of things: Model 31 load cell,” <https://sensing.honeywell.com/060-1426-02-miniature-stainless-steel-load-cells>, Accessed November 23, 2017.
- [16] Mitsubishi electric, “Servo motor,” www.mitsubishielectric.com/fa/products/cnt/cnc/items/servo/index.html, Accessed November 23, 2017.
- [17] NI, “Motion controller device,” <https://www.ni.com/en-us/shop/select/motion-controller-device?modelid=122652>, Accessed November 23, 2017.
- [18] NI Labview, “LabVIEW,” <https://www.ni.com/en-us/shop/labview.html>, Accessed November 23, 2017.

- [19] Ketcham, R., (2012). “X-ray computed tomography (CT),”
https://serc.carleton.edu/research_education/geochemsheets/techniques/CT.html,
 Science Education Research center, Carleton college, Accessed December 11,
 2017.
- [20] Robert, E., Djordjevic, B.B. and Hentschel, M.P., (2003). “Nondestructive characterization of Materials,” *Springer Science & Business Media*, **11**, 47-52.
- [21] Wilde, F., Ogurreck. M., Greving, I., Hammel, J.U., Beckmann, F., Hipp, A., Lottermoser, L., Khokhriakov, I., Lytaev, P., Dose, T., Burmester, H., Muller, M. and Schreyer, A., (2016), *AIP Conference Proceedings*, **1741**, 030035.
- [22] Mouritz, A.P., Bannister, M.K., Falzon, P.J. and Leng, K.H., (1999). “Review of applications for advanced three-dimensional fiber textile composites,” *Composite A*, **30**, 1445-1461.
- [23] Octopus Imaging Software, Ver. 8, XRE, Gent, Belgium, 2017.
- [24] Amira Software, Ver. 6.2, Thermo Fisher Scientific, Hillsboro, OR, 2017.
- [25] Schmidt, S., Beyer, S., Immich, H., Knabe, H., Meistring, R. and Gessler, A., (2005). “Ceramic matrix composites: A challenge in space propulsion technology applications,” *International Journal of Applied Ceramic Technology*, **2**, 85-96.
- [26] Marshall, D.B. and Cox, B.N., (2008). “Integral textile ceramic structures,” *Annual review of Material Research*, **38**, 425-443.
- [27] Morscher, G.N. and Pujar, V.V., (2009). “Design guidelines for in-plane mechanical properties of SiC fiber-reinforced melt-infiltrated SiC composites,” *International Journal of Applied Ceramic Technology*, **6**, 151-163.
- [28] Zhao, J.C and Westbrook, J.H., (2003). “Ultrahigh-temperature materials for jet engines,” *Material Research Bulletin*, **28**, 622-630.

- [29] Sarin, P., Yoon, W. and Jurkschat, K., (2006). “Quadrupole lamp furnace for high temperature (up to 2050 K) synchrotron power X-ray diffraction studies in air in reflection geometry,” *Review of Scientific Instruments*, **77**, 093906.
- [30] Guesdon, C., Alxneit, I., Tschudi, H.R., Wuillemin, D. and Sturzenegger, M., (2006). “1 kW imaging furnace with in situ measurement of surface temperature,” *Review of Scientific instruments*, **77**, 035102.
- [31] Watanabe, A. and Shimazu, M., (1976). “High-temperature X-ray diffraction furnace using a thermal-image technique,” *Journal of Applied Crystallography*, **9**, 466-469.
- [32] MacDowell, A.A., Parkinson, D.Y., Haboub, A., Schaible, E., Nasiatka, J.R., Yee, C.A., Jameson, J.R., Ajo-Franklin, J.B., Brodersen, C.R. and EcElrone, A.J., (2012). “X-ray micro-tomography at the advanced light source,” *The International Society for Optical Engineering*, **8506**, 850618-2.
- [33] Haboub, A., Bale, H.A., Nasiatka. J.R., Cox, B.N., Marshall, D.B., Ritchie, R.O. and MacDowell A.A., (2014). “Tensile testing of materials at high temperatures above 1700°C with in situ synchrotron X-ray micro-tomography,” *Review of scientific instrument*, **85**, 083702.
- [34] Corman, G.S. and Luthra, K.L., (2005). “Handbook of Ceramic Composites,” *Springer*, 99-115.
- [35] International light technologies, “Reflectors & reflector lamp assemblies,” <https://www.intl-lighttech.com/applications/reflectors-reflector-lamp-assemblies>, Accessed November 23, 2017.
- [36] TDK lambda, “ZUP-series,” www.tdk-lambda.com/products/sps/ps_adj/zup/indexe.html, Accessed November 23, 2017.

- [37] Omega engineering, “Fine gage Bare Wire Thermocouple Elements, J, K, T, E, N, R & S,” https://www.omega.com/pptst/IRCO_CHAL_P13R_P10R.html, Accessed November 23, 2017.
- [38] Luma sense technologies, “IMPAC Pyrometer IGA6 Advanced,” www.lumasenseinc.com/EN/products/temperature-measurement/infrared-thermometers/impac-pyrometers/series-6/pyrometer-impac-iga-6-advanced.html, Accessed November 23, 2017.
- [39] Patel, M., Saurabh, K., Prasa, V.V.B., and Subrahmanyam, J., (2011). “ High temperature C/C-SiC composite by liquid silicon infiltration: a literature review,” *Bulletin of Material Science*, **35**, 63-73.
- [40] Bruker, “Skycan 1176: high-resolution *in-vivo* mirco-CT,” www.bruker-microct.com/products/1176.htm, Accessed November 23, 2017.
- [41] Buehler, “IsoMet™ low speed precision cutter,” <https://www.buehler.com/isoMet-low-speed-cutter.php>, Accessed November 23, 2017.

ACKNOWLEDGEMENTS

Thank all those who have helped me,

First of all, I am grateful to my family members, my parents and brother. They always support and encourage me both materially and spiritually.

I would like to express appreciation to my advisor Professor Wooseok Ji for his endless guidance, support, and encouragement through my M.S. study at the UNIST. Especially, I was greatly impressed by his deep passion as a researcher. He also gave me the opportunity to study in the good research environment, and it was invaluable experience for me to grow further, and again, thank him.

I am also extremely grateful to all the members of my committee, Professor Han-Gi Chae, and Doctor Jae-Hong Lim for their help and serving as my committee members even with their busy schedule. Additionally, I thank them for comments and suggestions improving my thesis.

I would like to thank all CMS Laboratory members: Hee-young Choi, Hye-gyu Kim, Soo-young Lee, and Tae-seong Choi for their cooperation. My graduate life was very happy and not lonely because they let me smile, it has been lucky to meet with CMS lab members.

I am grateful to the technical support for experiments: Seob-Gu Kim in Pohang Accelerator Laboratory, Junyeon Hwang and Seung-gyu Park in KIST. It would never have been possible to complete this master's thesis without the help, guidance and support of these people.

Finally, I would like to thank for the financial support of the Lockheed Martin in the year of 2015 and Doosan Heavy Industry in the year of 2017.

Again, Thank all UNISTARs